THE ASTROPHYSICAL JOURNAL, 304:115–139, 1986 May 1

RAPIDLY ROTATING NEUTRON STAR MODELS

JOHN L. FRIEDMAN
Department of Physics, University of Wisconsin-Milwaukee

JAMES R. IPSER
Department of Physics, University of Florida

AND

LEONARD PARKER
Department of Physics, University of Wisconsin-Milwaukee
Received 1985 July 8; accepted 1985 October 28

ABSTRACT

Results are reported from a numerical investigation of the structure of rapidly rotating relativistic models, based on equations of state proposed for neutron star matter. Sequences of rotating stars with baryon mass approximately equal to 1.4 $M_{\odot}$ were constructed using 10 equations of state (EOSs) drawn from the Arnett-Bowers collection, together with the more recent Friedman-Pandharipande EOS; along each sequence the angular velocity increases from zero to the Keplerian frequency that marks the termination point. A number of additional sequences at other masses were constructed for a smaller set of EOSs spanning the full range of compressibilities. Because all sequences ended before the ratio $T/|W|$ of rotational energy to gravitational energy reached 0.14, instability to a bar mode appears unlikely. For the four stiffest EOSs, the upper limit on rotation set by gravitational instability to modes with angular dependence exp $(im\phi)$ for $m = 3$ and 4 (or by sequence termination) is consistent with the observed frequency of the fast pulsar. Upper limits on mass, baryon mass, moment of inertia, red- and blueshifts, equatorial velocity, and on the parameter cJ/GM^2 are found for representative EOSs. Lower limits on mass and central density are found for models rotating at the fast pulsar's frequency. Quantities characterizing models along each sequence are presented in tables, and a series of graphs illustrates metric components, density profiles, and surface embeddings for selected models.

Subject headings: dense matter — equation of state — stars: neutron — stars: rotation

I. INTRODUCTION

In 1978, Papaloizou and Pringle predicted the possible existence of a class of rapidly rotating neutron stars, arising when old neutron stars (with weak magnetic fields) are spun up by accretion. If the magnetic field is less than about 10^{10} G, rotation appears to be limited by a nonaxisymmetric instability driven by gravitational radiation (Friedman and Schutz 1978; Friedman 1978). Papaloizou and Pringle therefore suggested that accreting neutron stars might hover at an angular velocity for which the angular momentum gained in accretion balanced that lost to gravitational waves; Wagoner (1984) has analyzed the gravitational radiation produced by such systems, emphasizing that they might provide detectable sources of monochromatic waves. A number of authors have noted that the fast pulsar PSR 1937+214 may itself rotate at the limiting frequency (Fabian *et al.* 1983; Arons 1983; Cowsik, Ghosh, and Melvin 1983; Harding 1983; Ray and Chitre 1983; Friedman 1983; Wagoner 1984), and its discovery has renewed interest in the structure of rotating neutron stars.

Relativistic models of slowly rotating neutron stars were constructed by Hartle and Thorne (1968), using a formalism developed by Hartle (1967). Recently, similar calculations, using the same formalism, were performed by Datta and Ray (1983), to construct models based on a variety of proposed equations of state. An extensive study of the properties of these models has been made by Datta, Ray, and Kapoor (Datta 1984; Ray and Datta 1984; Kapoor and Datta 1984; Datta and Kapoor 1985; Datta, Kapoor, and Ray 1984). Previous models of *rapidly* rotating relativistic stars have been based on incompressible fluids and polytropic equations of state (Wilson 1972; Bonazzola and Schneider 1974; Butterworth and Ipser 1976; Butterworth 1976), and on dust (Bardeen and Wagoner 1971).

We report here results of the first numerical construction of rapidly rotating relativistic models based on equations of state (EOSs) proposed for neutron star matter. Over 400 models have been constructed to portray the structure of rapidly rotating neutron stars corresponding to a range of possible masses, frequencies of rotation, and compressibilities. Particular emphasis was given to establishing upper limits on rotation, mass, baryon mass, moments of inertia, redshifts, and blueshifts. We used 10 EOSs from the Arnett-Bowers (1977) study (hereafter A-B) of nonrotating models (see also Arnett and Bowers 1974), together with the more recent Friedman-Pandharipande (1981) EOS. A large part of the work was devoted to models based on four of these EOSs, chosen to span the range of compressibility: In the Arnett-Bowers notation, these were EOSs C (Bethe-Johnson I 1974), G (Canuto-Chitre 1974), L (Pandharipande-Smith 1975, mean field), and the Friedman-Pandharipande EOS (FP). Preliminary results of our study were announced in an earlier paper (Friedman, Ipser, and Parker 1984). Our numerical code is based on the programs developed by Butterworth and Ipser (1976) and used by Ipser to construct rotating polytropes. Two adaptations of these codes were independently developed (by Friedman and Parker, and by Ipser). Corresponding models from the two codes are in good agreement.

The plan of the paper is as follows. In § II we review briefly the relativistic description of rotating stars, establishing conventions and notation. A similarly brief discussion is presented of the numerical methods we used and their expected accuracy. Section III is devoted to upper limits on neutron star rotation: a hard upper limit is set by sequence termination, where the star's angular velocity Ω is equal to the angular velocity Ω_κ of a particle in circular orbit at the equator; a second, more stringent, limit is set by the gravitational instability referred to earlier. Recent work on the stability points (zero-frequency modes) of Newtonian polytropes (Imamura, Durisen, and Friedman 1985; Managan 1985) establishes critical values of the parameter t, the ratio T/W of rotational kinetic energy to gravitational binding energy, at which instability sets in. These values, together with a numerical determination of the relation between t and the angular velocity Ω for our models, is used to estimate the stability limits of Ω for each EOS. In § IV we examine models at termination for five representative EOSs: C, F, FP, G, and L, to find upper limits on mass, baryon mass, moment of inertia, and red- and blueshifts for each EOS. For these EOSs and a version of EOS N (see § II), several sequences of models with angular velocity ranging from zero to $\Omega = \Omega_\kappa$ were constructed; tables and graphs describing these models are presented here. Finally, in § V we discuss astrophysical implications of our results.

We use lower case italic letters for spacetime indices and adopt the metric signature $-+++$. Values of physical constants used in our numerical work conform to those of A-B: $c = 2.9979 \times 10^{10}$ cm s^{-1}, $G = 6.6732 \times 10^{-8}$ g^{-1} cm^3 s^{-2}, $M_\odot = 1.987 \times 10^{33}$ g.

II. ROTATING RELATIVISTIC STELLAR MODELS

Our neutron star models are uniformly rotating, axisymmetric perfect fluid configurations. Because the proposed equations of state describe zero-temperature matter, they have the form $\epsilon = \epsilon(p)$, where ϵ and p are, respectively, the energy density and pressure of the fluid, measured by a comoving observer. The spacetime is stationary and axisymmetric with Killing vectors t^a and ϕ^a corresponding to time translation and rotation. The fluid's 4-velocity can be written as a linear combination

$$u^a = t^a + \Omega\phi^a , \tag{1}$$

where Ω is the angular velocity (measured by an observer at infinity at rest relative to the star).[1]

There are unique scalars t and ϕ for which $\nabla^a t$ and $\nabla^a\phi$ lie in the plane of t^a and ϕ^a, and which satisfy

$$t^a\nabla_a t = \phi^a\nabla_a\phi = 1 ; \quad t^a\nabla_a\phi = \phi^a\nabla_a t = 0 . \tag{2}$$

In terms of these and coordinates $\bar{r}$ and θ on a surface of constant t and ϕ, the spacetime metric g_{ab} can be written in the form

$$ds^2 = -e^{2\nu}dt^2 + e^{2\psi}(d\phi - \omega dt)^2 + e^{2\mu}(d\bar{r}^2 + \bar{r}^2 d\theta^2) , \tag{3}$$

with metric coefficients independent of t and ϕ. We will use the unbarred letter r to denote the (Schwarzschild-like) radial coordinate in the equatorial plane for which $2\pi r$ is the proper circumference of a circle concentric to the equator: $r = e^\psi$. (In the Butterworth-Ipser papers, e^ψ and e^μ are written, following Bardeen and Wagoner 1971, in terms of functions B and ζ: $e^\psi = \bar{r}B \sin\theta e^{-\nu}$, $e^\mu = e^{\zeta-\nu}$.)

[1] To simplify the equations, we have set $c = 1$ in § II. In the remainder of the text, c has not been suppressed.

The stellar model satisfies the field equation

$$G_{ab} = 8\pi G T_{ab} , \tag{4}$$

where

$$T_{ab} = \epsilon u_a u_b + p(g_{ab} + u_a u_b) \tag{5}$$

is the energy-momentum tensor of the fluid. Equation (4) and the Bianchi identity imply the equation of hydrostatic equilibrium

$$(g_{ab} + u_a u_b)\nabla_c T^{bc} = 0 ,$$

which, for a uniformly rotating, isentropic fluid, has the first integral

$$h(p) = \ln(\beta^{1/2}/u^t) . \tag{6}$$

The quantity $h(p)$ is the comoving enthalpy density

$$h(p) = \int^p dp/(\epsilon + p) , \tag{7}$$

and

$$\beta = e^{2\nu}\Big|_{\text{pole}}$$

is the injection energy of a unit mass particle lowered from infinity to the star. The injection energy is related to the polar redshift z_p by

$$z_p = \beta^{-1/2} - 1 .$$

Note that the possibility of an extensive solid crust or core in neutron stars has negligible effect on their structure in the sense of their pressure and density distributions and gravitational potentials. The reason is that the ratio of anisotropic stresses to the isotropic pressure is comparable to the ratio of the largest deviation of the surface from the shape of an equilibrium field—that is, to the fractional change in radius during the largest glitches, about 10^{-6}. The normal mode frequencies and their instability points are similarly unaffected by the very small departures from a perfect fluid equilibrium that the anisotropic stresses permit.

a) *Numerical Method*

A detailed discussion of the numerical method we follow is given in Butterworth and Ipser (1976). They generalize Stoeckly's (1965) work on rotating Newtonian polytropes to the substantially more complex relativistic stellar structure equations. Briefly, one uses the Newton-Raphson method to successively approximate the solution (g_{ab}, p) to equation (4) with $\epsilon = \epsilon(p)$ and with u^a given by equation (1). As a zeroth approximation, one takes a previously constructed model (${}^0g_{ab}$, ${}^0p$) with values of angular velocity and injection energy close to (typically smaller than) those of the model to be computed. One then recomputes the pressure, using the integrated equation of hydrostatic equilibrium with the desired values of angular velocity and injection energy and solves components of the perturbation equations

$$\delta G_{ab} - 8\pi G\delta T_{ab} = G_{ab}({}^0g) - 8\pi G T_{ab}({}^0g, {}^1p) \tag{8}$$

for the perturbed potentials δg_{ab}, where δG denotes the change in G due to a change δg in the metric. In this way one obtains a first-order approximation (${}^1g_{ab}$, ${}^1p$) to the solution. The $(n+1)$th approximation is then obtained from the nth by first solving the equation of hydrostatic equilibrium (6) to find ${}^{n+1}p$ in terms of ${}^{n}g_{ab}$ and then solving equation (8) to find ${}^{n+1}g_{ab} = {}^{n}g_{ab} + \delta g_{ab}$ in terms of ${}^{n+1}p$ and ${}^{n}g_{ab}$. The actual program is slightly different: to avoid inverting the large matrix of coefficients that corresponds to the linear operator on the left-hand side of equation (8), one solves individual equations of equation (8) one by one for individual perturbed potentials ($\delta\gamma$, $\delta\omega$, δB, $\delta\zeta$) and recomputes p from the hydrostatic equilibrium equation after finding each potential.

b) *Equations of State*

All but two of the EOSs used in our models were taken from the collection used by A-B; several of these appear also in the Baym-Pethick (1979) review article, and subsequent authors (e.g., Shapiro and Teukolsky 1984; Ray and Datta 1984) have adopted the Baym-Pethick notation. Each EOS will be referred to by the letter (A–G, L–O) used by Arnett and Bowers, and when applicable by the Baym-Pethick abbreviation (in parentheses). We denote by N*(RMF) the modification due to Serot (1979*a*, *b*) of Walecka's (1974) EOS based on a relativistic mean field approximation (this latter is EOS N of A-B); nonrotating neutron star models based on N*(RMF) are given by Detweiler and Lindblom (1977). The EOSs we use are then

A(R)	Reid soft core, Pandharipande (1971*a*)
B	Reid core with hyperons, Pandharipande (1971*b*)
C(BJ I)	Bethe and Johnson (1974), model I
D(BJ V)	Bethe and Johnson (1974), model V
E	Mozkowski (1974)
F	Arponen (1972)
G	Canuto and Chitre (1974)
L(MF)	Mean field, Pandharipande and Smith (1975)
M(TI)	Tensor interaction, Pandharipande and Smith (1975)
N*(RMF)	Relativistic mean field, Serot (1979)
O	Bowers, Gleeson, and Pedigo (1975)
FP	Three-nucleon interactions, Friedman and Pandharipande (1981)

As described by Friedman and Pandharipande (1981), the FP EOS agrees with that of Negele and Vautherin (1973) for baryon number density $n < 0.1$ fm^{-3} and with the Baym-Pethick-Sutherland (1972) EOS for $n < 0.001$ fm^{-3}. EOS N*(RMF) agrees with Baym-Pethick-Sutherland at $n \leq 0.1$ fm^{-3}. We did not construct models based on an EOS exhibiting pion condensation; but the "π" models considered in Baym and Pethick (1979) are intermediate in stiffness between EOSs G and A(R), and similar to EOS B. It is in general helpful in interpreting our results to have available an ordering of the EOSs used in terms of their stiffness. Because $dp/d\rho$ varies with density, there is no unambiguous order, but two measures of average stiffness have particular relevance. The first is the maximum mass of spherical models based on a given EOS: from softest (smallest mass) to stiffest (largest mass), the order is G, B, F, D, A, E, C, M, FP, O, N, L. A second measure, more appropriate for comparison of 1.4 $M_\odot$ models, is the radius at fixed baryon mass, $M_0 = 1.4\ M_\odot$: here the order from softest (smallest radius) to stiffest (largest radius) is G, B, A, E, F, D, FP, C, O, N, L, M.

Four-point Lagrange interpolation was used to interpolate values of $\log p$, $\log \epsilon$, $\log h$, and $\log \rho$, where $\rho = n\mu_B$ is the baryon mass density measured by a comoving observer, n is the baryon number density, and μ_B is the mass per baryon, taken as 1.659×10^{-24} g, to agree with A-B conventions. The enthalpy density was found by numerical integration of eq. (7).

c) *Mass, Angular Momentum, Red- and Blueshifts, Surface Embedding*

Let n^a be a unit vector orthogonal to a hypersurface of constant t, and let dV be the proper volume element of the surface. Integral quantities characterizing a rotating neutron star include its gravitational mass,

$$M = \int (T_{ab} - \tfrac{1}{2} g_{ab} T) t^a n^b dV \ , \tag{9}$$

its angular momentum,

$$J = \int T_{ab}\, \phi^a n^b dV \ , \tag{10}$$

and its baryon mass,

$$M_0 = \int \rho u_a n^a dV \ . \tag{11}$$

Its moment of inertia is defined by

$$I = J/\Omega \ .$$

Shifts in the frequency of light emitted from the equator and the poles are tabulated for the calculated models. To find the shifts for a photon with 4-momentum p_a, note that the energy $p_a t^a$ and angular momentum $p_a \phi^a$ are constant along a photon trajectory. For light emitted forward (backward) at the equator,

$$p^a = \text{const} \times [t^a + (\omega \pm e^{\nu-\psi})\phi^a] \ , \tag{12}$$

and the emitted frequency is $\omega_E = p_a u^a$, where u^a is the fluid 4-velocity at the equator:

$$u^a = \frac{e^{-\nu}}{\sqrt{1-v^2}} (t^a + \Omega \phi^a) \ , \tag{13}$$

with

$$v = (\Omega - \omega) e^{\psi - \nu}$$

(v is the fluid velocity measured by a zero angular momentum observer). Because a distant observer at rest relative to the star moves along the timelike Killing vector, the frequency observed at infinity is $\omega_\infty = p_a t^a$. Then

$$\frac{\omega_\infty}{\omega_E} = \frac{p_a t^a}{p_a u^a} = e^{\nu} \left(\frac{1 \mp v}{1 \pm v} \right)^{1/2} (1 \pm e^{\psi-\nu}) \ . \tag{14}$$

The polar redshift is easier to obtain: an observer at the pole has 4-velocity $u^a = t^a / |t^b t_b|^{1/2} = t^a / |g_{tt}|^{1/2}$. The fact that $t^a \propto u^a$ implies that the polar redshift is independent of the photon's direction:

$$\frac{\omega_\infty}{\omega_E} = \frac{p_a t^a}{p_a u^a} = \sqrt{|g_{tt}|} \ . \tag{15}$$

We denote by z_p, z_B, and z_F the red- (or blue)shifts of light emitted at the pole and in the backward and forward directions at the equator:

$$z = \frac{\omega_E}{\omega_\infty} - 1 \ . \tag{16}$$

In § IV, we present several embedding diagrams, graphs that depict the intrinsic geometry of the stellar surfaces. Given a surface $r = r(\theta)$, in a t = constant slice of spacetime, one constructs an embedding as follows. The metric of the stellar surface induced by the spacetime metric (3) is

$$d\sigma^2 = e^{2\psi}d\phi^2 + e^{2\mu}\left[\left(\frac{d\bar{r}}{d\theta}\right)^2 + \bar{r}^2(\theta)\right]d\theta^2 , \quad (17)$$

and we want to find a surface in a flat three-dimensional space whose geometry is given by the 2-metric (17). Let ϖ, z and ϕ be cylindrical coordinates for the flat space and $\varpi = \varpi(z)$ the embedded surface. From the flat metric,

$$d\varpi^2 + dz^2 + \varpi^2 d\phi^2 ,$$

the surface inherits a 2-metric

$$d\sigma^2 = \left[\left(\frac{d\varpi}{dz}\right)^2 + 1\right]dz^2 + \varpi^2 d\phi^2 ,$$

which agrees with the star's surface geometry if

$$\varpi = e^{\psi}$$

and

$$z = \int (d\sigma^2 - d\varpi^2)^{1/2} . \quad (18a)$$

More explicitly, with $\varpi(\theta) = e^{\psi}[r(\theta), \theta]$,

$$z(\theta) = \int_0^{\theta} d\theta \left\{ e^{2\mu}\left[\left(\frac{d\bar{r}}{d\theta}\right)^2 + \bar{r}^2\right] - \left(\frac{d\varpi}{d\theta}\right)^2 \right\} .$$

The equatorial and polar radii of the embedded surface are given by

$$r_{\rm eq} = \varpi\left(\theta = \frac{\pi}{2}\right) , \quad r_p = z(\theta = 0) . \quad (18b)$$

We define the eccentricity e by

$$e = (1 - r_{\rm eq}^2/r_p^2) , \quad (19)$$

in agreement with the usual definition when the surface has the geometry of an ellipsoid. For slow rotation, the surface *is* an ellipsoid to $O(\Omega^2)$ and e is then its true eccentricity.

d) Numerical Accuracy

A variety of internal checks and a few external comparisons provide a good picture of the code's accuracy. Changing the number of spokes from 6 to 15 altered no quantity by more than 0.1% in the several models we compared: metric coefficients, energy density, integral properties, radii, and redshifts were compared in models with the same angular velocity and injection energy. Changing the number of radial grid points from 60 to 40 similarly altered the potentials and the integral quantities of the models by less than 0.1%; but radii and quantities that depend on the radii (redshifts and equatorial velocities) changed by up to 5%. Similar changes in the radii and related quantities resulted from changing the number of grid points used to extrapolate to zero pressure along a radial direction. When the interpolation method used to obtain $\epsilon(p)$, $n(p)$, and $h(p)$ from the tabulated equation of state was changed from four-point Lagrange interpolation to a cubic spline fit, changes in all quantities were at the 0.1% level.

The present code was compared with the earlier Ipser-Butterworth program for rotating polytropes, by constructing $n = 3/2$ relativistic polytropes with the same injection energy and angular velocity, and agreement was obtained to six places, the expected accuracy of the computer and of the iteration. (For the accuracy tests, convergence of the iterations to one part in 10^5 or 10^6 was demanded; for most models, convergence to one part in 10^3 or 10^4 was standard). Finally, for the rotating $n = 3/2$ polytropes, agreement to within 1% was obtained in a comparison of slowly rotating models with Hartle's models constructed from his slow-rotation formalism.

To summarize, we regard the metric coefficients, density and pressure distributions, and masses of our models as accurate to $\sim 1\%$, while the determination of the stellar surface and of quantities that directly depend on it is not much more accurate than the radial grid spacing; that is, the radii, redshifts, and equatorial velocities tabulated below have expected errors of $\sim 5\%$.

III. UPPER LIMITS ON NEUTRON STAR ROTATION

When the magnetic field of a neutron star is sufficiently weak, its rotation is apparently limited by a gravitational instability to nonaxisymmetric perturbations. Gravitational radiation makes all rotating, perfect fluid equilibria unstable to modes with angular dependence exp $(im\phi)$ for sufficiently large m, allowing the star to convert its rotational energy to gravitational waves (Friedman and Schutz 1978; Friedman 1978). The instability sets in when a backward-traveling mode is dragged forward relative to an inertial frame by the star's rotation. Relative to a comoving observer, the mode continues to move in a sense opposite to the star's rotation, and the perturbed star thus has smaller angular momentum than the unperturbed configuration. In other words, the perturbation still has negative angular momentum. However, because gravitational radiation now carries off positive angular momentum while the perturbation's angular momentum remains negative, the radiation drives the perturbation instead of damping it. The Dedekind bar instability found by Chandrasekhar (1970) is the $m = 2$ case of this mechanism, but higher modes are unstable first, and we will see that neutron stars appear always to reach Keplerian velocity before the $m = 2$ mode is unstable.

In realistic models, the instability for large m is damped out by viscosity when the dissipation due to viscosity is equal to the loss of energy to gravitational waves (Lindblom and Detweiler 1977; Detweiler and Lindblom 1977; Comins 1979; Lindblom and Hiscock 1983). In the case of neutron stars, the instability can be expected to play a role only for old stars spun up by accretion or for newly formed stars. In either case, because the star is hot, viscosity will be relatively small (see § V*a*); viscous dissipation should stabilize modes with $m > 5$; and the $m = 3$ and $m = 4$ (or possibly $m = 5$) modes can be expected to set the limit on neutron star rotation (Friedman 1983; Wagoner 1984). Imamura, Durisen, and Friedman (1985) and Managan (1985) have recently determined the gravitational-radiation instability points for Newtonian polytropes in terms of the parameter $t = T/|W|$. The adiabatic index governing the perturbations was assumed identical to the equilibrium value of $d \log p/d \log \epsilon = 1 + 1/n$, where n is the polytropic index. As exhibited in Table 1, the critical values t_3 and t_4 of t at which the $m = 3$ and $m = 4$ modes become unstable were found to increase with increasing stiffness, taking their maximum values for the incompressible ($n = 0$) Maclaurin models. The Maclaurin values can be interpolated from

TABLE 1

INSTABILITY POINTS OF UNIFORMLY ROTATING POLYTROPES

n	t_3	t_4
0	0.099	0.077
0.5...............	0.096	0.074
1	0.080	0.058
1.5...............	0.059	0.043

Comins' (1979) tables; precise values are given by Baumgart and Friedman (1985).

The compressibility of neutron star matter (in the proposed equations of state) corresponds to a polytropic index between 0.5 and 1.5. A relativistic analog of t can be defined by setting

$$T = \tfrac{1}{2}J\Omega \tag{20}$$

and

$$W = M_p c^2 + T - Mc^2 , \tag{21}$$

where we have split the mass (energy) M of a star into rotational kinetic energy T, binding energy W, and proper mass

$$M_p = \int \epsilon u^a n_a dV . \tag{22}$$

Because the growth time for the gravitational instability increases very rapidly when the mode's frequency is near zero (near the instability point) (Comins 1979), viscosity can be expected to stabilize the $m = 4$ mode when $t - t_4 < 0.03$. Assuming that the Newtonian values of t_3 and t_4 approximate their relativistic values, instability would then set in at $t \approx 0.08$. We find that *the value of the angular velocity at the instability point is insensitive to t and for a given EOS can be accurately determined despite the uncertainty in the value of t.* In particular, even if viscosity damps the instability altogether, so that the limit on rotation is set by the Kepler frequency, the value of the limiting frequency is not greatly altered.

Figures 1–4 show the relation between t and Ω for sequences of neutron stars parameterized by increasing Ω. The endpoint of each sequence, marked by a dot, represents a star rotating at the Kepler frequency Ω_K: the frequency of a particle in circular orbit at the equator. For the metric (3),

$$\Omega_K = e^{\nu-\psi}v + \omega , \tag{23a}$$

where

$$v = \frac{\omega'}{2\psi'} e^{\psi-\nu} + \left[c^2 \frac{\nu'}{\psi'} + \left(\frac{\omega'}{2\psi'} e^{\psi-\nu}\right)^2\right]^{1/2} \tag{23b}$$

is the orbital velocity measured by an observer with zero angular momentum in the ϕ-direction, and all potentials are evaluated at the equator. (Primes denote derivatives with respect to a radial coordinate, $\bar{r}$ or ϖ). Because no uniformly rotating star can have $\Omega > \Omega_K$, the Kepler frequency sets a hard upper limit on rotation. Sequences of $M_0 = 1.4\ M_\odot$ models were constructed for EOSs D(BJ V) and E as well, but the results are not included in Figure 1. The t versus Ω curves for EOSs D, E, and FP all lie between the curves for EOSs C(BJ I) and F. The curve for EOS E lies slightly above that of FP, terminating at $t = 0.099$. The curve for EOS D nearly coincides with the FP curve but terminates at $t = 0.095$.

A striking feature of the $M_0 \approx 1.4\ M_\odot$ models (Fig. 1) is that $t(\Omega = \Omega_K) < 0.13$ for all EOSs. It is therefore unlikely that neutron stars can rotate fast enough to be unstable to an $m = 2$ mode. Models with smaller masses (lower densities) are much softer, and the termination points occur dramatically earlier (see Tables 8–11), as one would expect from studies of rotating Newtonian polytropes (James 1964; see also Tassoul 1978, and references therein). The largest value of t occurs for EOS FP, which is unphysically stiff when $\epsilon > 10^{15}$ g cm^{-3} (for $\epsilon > 2 \times 10^{15}$ g cm^{-3}, the speed of sound exceeds the speed of light). Although a number of authors (Cowsik, Ghosh, and Melvin 1983; Harding 1983; Ray and Chitre 1983) have suggested that the fast pulsar may be at an $m = 2$ instability point,

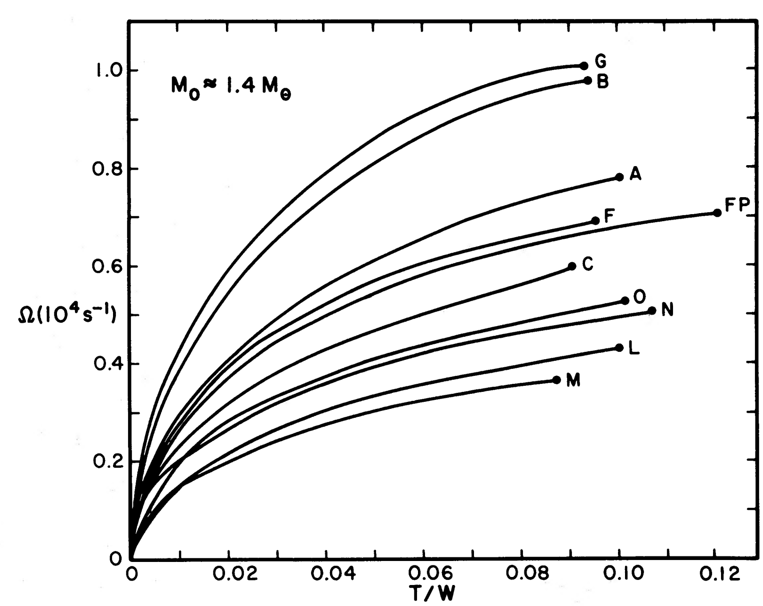

FIG. 1.—Angular velocity Ω vs. stability parameter $t = T/|W|$ for sequences of models with baryon mass $M_0 \approx 1.4\ M_\odot$. The curves are labeled by letters denoting equations of state, following the (Arnett-Bowers) notation introduced in § II. The injection energy β is constant along each sequence.

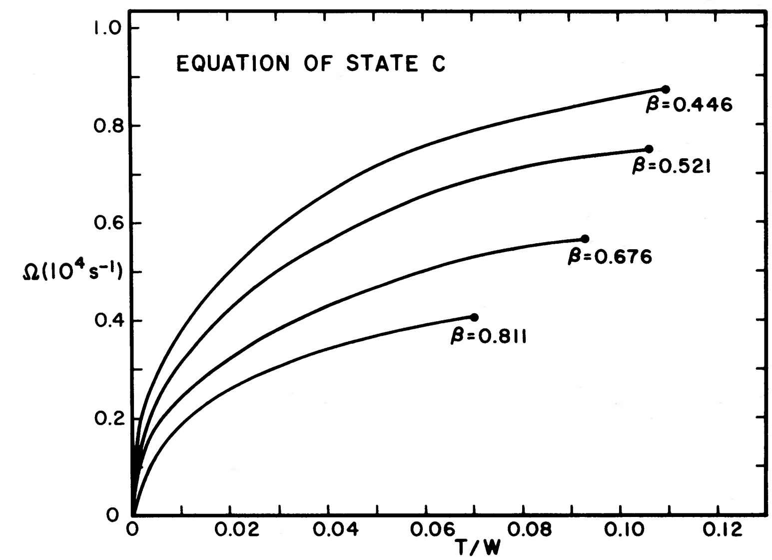

FIG. 2.—Ω vs. t for sequences of models based on EOS C(BJ I). Along each sequence, the injection energy β is held constant, and the corresponding curve is labeled by its value of β.

sequences of Newtonian stars of comparable stiffness ($n \geq 0.81$) similarly terminate before the bar mode is unstable.

The Keplerian frequency Ω_K at which a sequence terminates is substantially smaller than its value for the spherical model. As the rotation and hence the radius of a star increases, Ω_K decreases; at $\Omega = \Omega_K$, the Kepler frequency ranges from 55% of its spherical value for models based on the softest EOS to 75% of the spherical value for models with the stiffest EOS, L(MF).

Along each curve in Figures 1–4, the value of the injection energy (strictly, the value of β found from the first grid points outside the star) is held fixed. For the models of Figure 1, this is roughly equivalent to holding the baryon mass fixed at $M_0 = 1.4\ M_\odot$. If, as discussed above, we assume that neutron stars are unstable when $t > 0.08$, then the curves allow one to find the corresponding limiting frequencies of rotation. The curves are parabolas for small Ω, with

$$T = \frac{1}{2} \frac{I_0}{|W_0|} \Omega^2 ,$$

because to order Ω^2 the moment of inertia and gravitational binding energy retain the values I_0 and W_0 of the spherical model. However, as Ω approaches Ω_K, $I/|W|$ increases rapidly with Ω until $t \approx \Omega^{3.3}$ for $\Omega \approx \Omega_K$. As a result, the limiting value of Ω is insensitive to the precise value of t at which instability sets in.

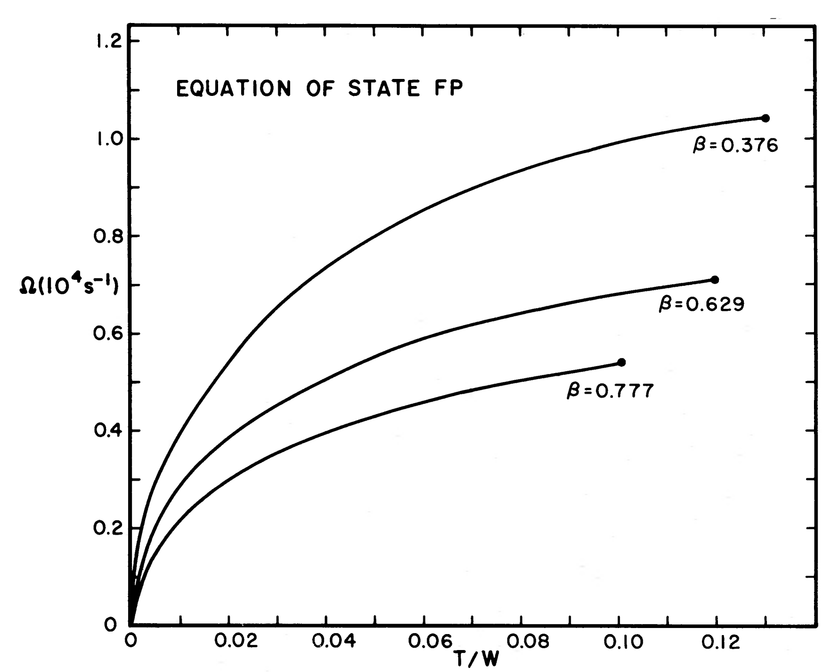

FIG. 3.—Ω vs. t for sequences of models based on EOS FP. As in Fig. 2, curves are labeled by the (constant) injection energy β.

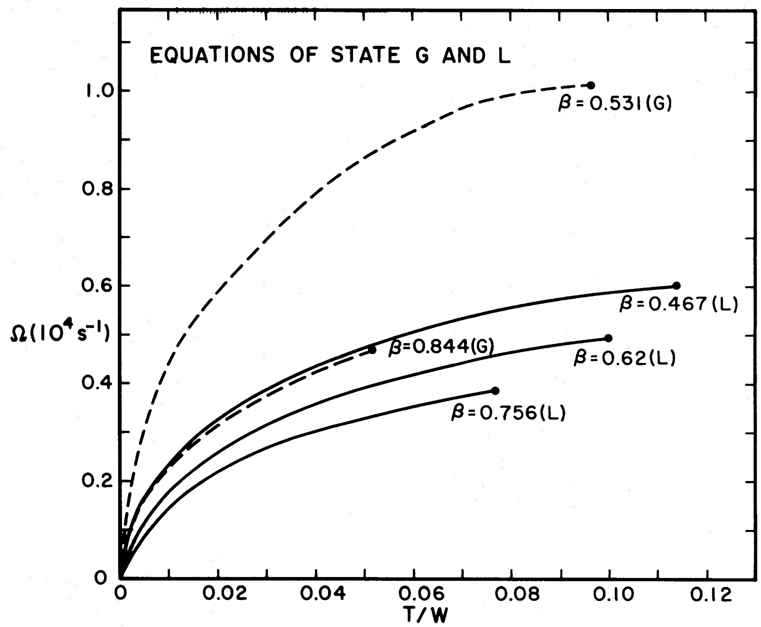

FIG. 4.—Ω vs. t for sequences of models based on EOS G and L(MF). Curves are again labeled by the (constant) injection energy β.

On the other hand, it is clear from Figure 1 that the limiting frequency depends strongly on the equation of state used. At $M_0 = 1.4\, M_\odot$, $\Omega(t = 0.08) < \Omega_{\rm lim} < \Omega_{\rm K}$ implies

$$\Omega_{\rm lim} = (9.9 \pm 0.2) \times 10^3\ {\rm s}^{-1}\ , \text{ for EOS G} \quad \text{(softest)}\ ,$$

$$\Omega_{\rm lim} = (5.8 \pm 0.6) \times 10^3\ {\rm s}^{-1}\ , \text{ for EOS C(BJ I) (intermediate)}\ ,$$

$$\Omega_{\rm lim} = (3.8 \pm 0.3) \times 10^3\ {\rm s}^{-1}\ , \text{ for EOS L(MF) (stiff)}\ .$$

The dependence of $\Omega_{\rm lim}$ on mass can be seen from the curves in Figures 2–4. For a given EOS, models with smaller β have larger mass and central density (see Tables 3–7 below). We find $(\partial \log \Omega)/(\partial \log M) \approx 1$ at fixed t. For EOS C(BJ I), for example, $\Omega_{\rm K}$ varies from 4.1×10^3 to $11 \times 10^3\ {\rm s}^{-1}$ as M changes from 0.78 to 2.16 $M_\odot$.

For the stiffer equations of state, the limiting frequency for stars with $M_0 = 1.4\, M_\odot$ is close to the frequency $\Omega_{\rm fp} = 0.4033 \times 10^4\ {\rm s}^{-1}$ of the fast pulsar. It is worth noting that the γ-ray burst data also favor stiff equations of state, if one interprets the observed emission lines as redshifted photons from e^+e^- annihilation occurring *at the surface* of neutron stars (Lindblom 1984). That is, the range of surface redshifts from neutron stars with $M = 1.2$–$1.4\ M_\odot$ is consistent with the observed redshift range only for the four stiffest EOSs: Models with a softer EOS have smaller radii (at fixed mass), and their surface redshifts are greater than those observed.

In § V, the t versus Ω curves are used to estimate growth times for the nonaxisymmetric instability.

IV. UPPER LIMITS ON MASS, BARYON NUMBER, MOMENT OF INERTIA, REDSHIFTS, AND BLUESHIFTS

a) Upper Limit on Mass and Baryon Number

By stiffening their response to compression, rotation stabilizes neutron stars, allowing more baryons to be added before the star collapses. The upper limit on baryon number and mass of rotating neutron stars is thus somewhat higher than for the corresponding spherical stars. For each equation of state, the equilibrium model with largest mass is a model rotating at the Keplerian frequency, $\Omega = \Omega_{\rm K}$. Somewhat stronger mass limits are implied by the requirement that the model be stable against the $m = 3$ and $m = 4$ modes, and these are discussed briefly below.

The change in the limiting mass is sharply constrained by the fact that neutron stars presumably cannot maintain differential rotation. In white dwarf models, the analogous effect of rotation on the upper mass limit has been studied in some detail. Although stable, differentially rotating dwarfs can have masses 2.5 times the Chandrasekhar limit for spherical stars (Durisen 1975), if one allows only uniform rotation, the upper mass limit is raised by at most 15% (James 1964). Because neutron stars are stiffer than dwarfs, their maximum rotation measured by dimensionless quantities (t or $\Omega/[\pi g \epsilon_c]^{1/2}$ is substantially larger. The change in the maximum mass, however, turns out to be only slightly higher than that for uniformly rotating dwarfs.

The mass limit of slowly rotating neutron stars was first considered by Hartle and Thorne (1968) and, more recently, Datta, Kapoor, and Ray (Datta and Ray 1983; Kapoor and Datta 1984; Datta and Kapoor 1985; Datta, Kapoor, and Ray 1984; Ray and Datta 1984) have used Hartle's slow rotation formalism to study the mass limit for rotating models based on a number of EOSs, including several we consider here. The latter authors assumed as an upper limit on rotation $\Omega_s = 0.52\Omega_0$, where $\Omega_0 = (Gc^{-2}M/R^3)^{1/2}$ is the frequency of a particle in circular orbit at the surface of the spherical model. Although this was an estimate of the (probably nonexistent) $m = 2$ instability point, the actual limiting frequencies we find vary (as noted in § III) from $0.55\Omega_0$ to $0.75\Omega_0$. However, the corresponding estimate of the change in maximum mass given by the slow rotation formalism turns out to be unexpectedly low. Our results do agree with a previous estimate of Shapiro and Lightman (1976), who analyzed post-Newtonian polytropes and found an expected fractional change in mass $\delta M/M \approx 0.2$.

Upper mass limits for models with $\Omega = \Omega_{\rm K}$ are listed in Table 2. We have chosen a representative sample of EOSs

TABLE 2

MAXIMUM-MASS MODELS[a]

Equation of State	β	Ω	ϵ_c (10^{15} g cm^{-3})	$M/M_\odot$	Increase	$M_0/M_\odot$	R	ω_c/Ω	T/W	V_{eq}/c	I (10^{45} g cm^2)	cJ/GM^2	e	Z_p	Z_B	Z_F
L	0.34	0.76	1.11	3.18	20%	3.72	17.3	0.77	0.122	0.53	7.87	0.68	0.69	0.71	2.08	−0.29
FP	0.28	1.23	2.5	2.30	17	2.71	12.	0.83	0.133	0.49	2.41	0.50	0.67	1.89	2.63	−0.32
C	0.35	1.11	2.7	2.16	17	2.47	13.	0.79	0.110	0.47	2.42	0.49	0.68	0.69	1.96	−0.32
F	0.39	1.24	4.1	1.66	13	1.87	11.	0.77	0.094	0.44	1.16	0.47	0.67	0.60	1.68	−0.29
G	0.34	1.52	5.5	1.55	14	1.73	8.6	0.81	0.101	0.43	0.86	0.62	0.62	0.71	2.01	−0.29

[a] Properties of uniformly rotating models with maximum possible mass, for various equations of state.

ranging from the stiffest (L) to the softest (G) models in the A-B collection, together with models based on the more recent FP EOS. The fractional change in mass generally increases with increasing stiffness of the EOS, from 0.13 to 0.20. In contrast, the slow rotation results of Hartle and Thorne (1968) yield $\delta M = 0.17(\Omega/\Omega_0)^2 \leq 0.10$ (for each of their EOSs) when the limiting frequency is taken to be its largest value consistent with our results: $\Omega < \Omega_K < 0.75\Omega_0$. Similarly, Datta and Ray find $\delta M/M \leq 0.06(\Omega/\Omega_s)^2$, implying $\delta M/M \leq 0.11$ for $\Omega \leq \Omega_K$ when the value of Ω_K/Ω_s appropriate to each of their EOSs is used as the maximum value of Ω.

The key to the headings of Tables 2–13 is as follows:

β	Injection energy or, equivalently, value of the metric quantity $e^{2\nu}$ at the pole
Ω	Angular velocity relative to infinity (10^4 s^{-1})
ϵ_c	Central mass-energy density
$M/M_\odot$	Total mass
Increase	Percent increase of maximum mass over that for no rotation
$M_0/M_\odot$	Baryon (or rest) mass
R	Equatorial circumference radius ([proper equatorial circumference]/2π)
ω_c/Ω	Percentage of central dragging, as measured by central ratio of metric potential ω to Ω
T/W	Ratio of rotational energy to gravitational energy, as defined in § III
V_{eq}/c	Velocity of comoving observer at equator relative to locally nonrotating observer
I	Moment of inertia
cJ/GM^2	Dimensionless ratio of angular momentum J to M^2
e	Eccentricity, as defined by embedding technique discussed in § II*c*
Z_p	Polar redshift
Z_B	Equatorial redshift in backward direction
Z_F	Equatorial redshift in forward direction

In Figures 5–8 curves of mass versus radius are shown for EOSs C(BJ I), F, G, and L(MF). For each EOS, a sequence of spherical stars and one of stars with $\Omega = \Omega_K$ are portrayed. Along the $\Omega = \Omega_K$ sequences, the maximum mass model has somewhat lower density than the corresponding spherical model with maximum mass (see also Table 2). Rotation also flattens the curves because it preferentially increases the radius of low-density stars.

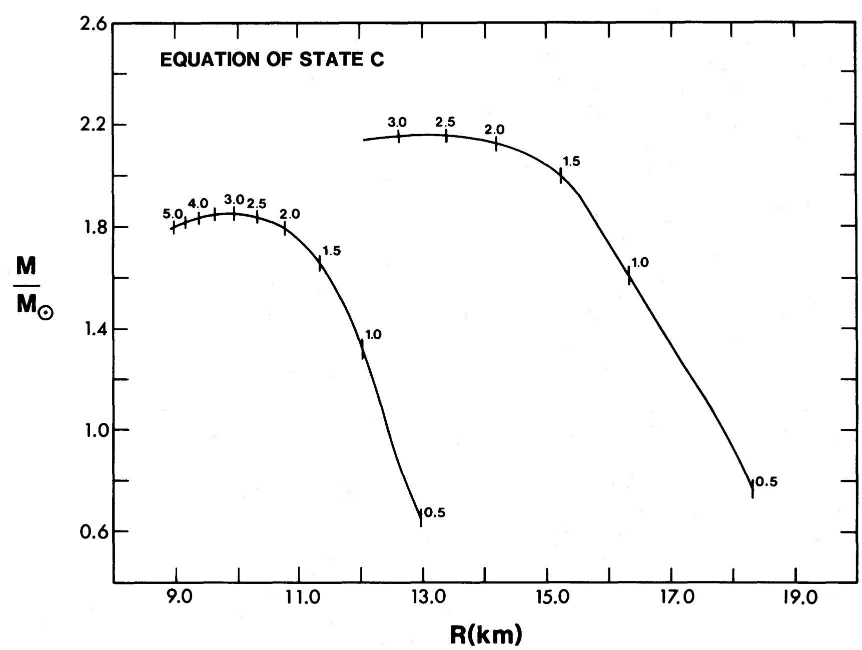

FIG. 5.—Gravitational mass vs. equatorial radius for two sequences of models based on EOS C(BJ I). One curve, with smaller values of the radii, describes spherical models, while the other describes models rotating with maximum (Keplerian) angular velocity ($\Omega = \Omega_K$). Along each curve, tick marks are labeled with the value of the models' central density in units of 10^{15} g cm^{-3}.

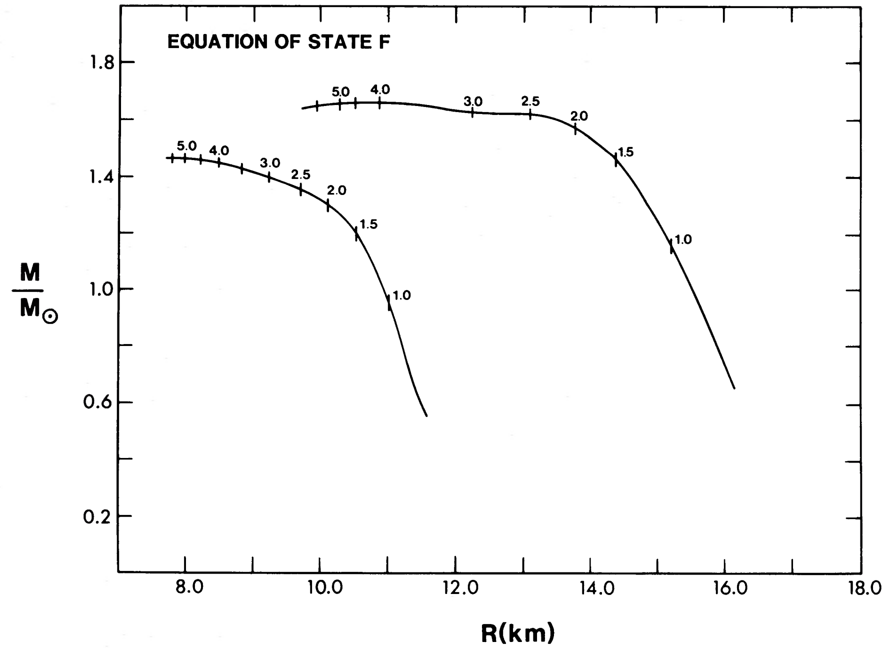

FIG. 6.—Gravitational mass vs. equatorial radius as in Fig. 5, for models based on EOS F

For spherical neutron stars, an instability to radial oscillation—to collapse—bounds the region of stable equilibria and sets an upper limit on their central density (Chandrasekhar 1964; Misner and Zapolsky 1964). In the approximation that the star's pulsation is governed by the same EOS $p = p(\epsilon)$ as is the equilibrium configuration, instability sets in *at* the upper mass limit (see Thorne 1967, and references therein). Adjoining any star beyond the maximum mass model ($\epsilon_c > \epsilon_c|_{M=M_{\max}}$) are nearby configurations with the same baryon number and with lower energy. If the same effective equation of state $p = p(\epsilon)$ governed both pulsations and the equilibrium star, then the lower energy configurations would be dynamically accessible. As it is, one expects stars just beyond the mass peak to be unstable but with a longer than dynamical time scale.

A similar "turning point" argument can be used to show that sequences of rotating stars with fixed angular momentum are unstable beyond the point where the mass (or, equivalently, baryon number) is a maximum (Friedman, Ipser, and Sorkin 1986). Again, the sequences can be parameterized by a star's central density, and as in the spherical case, what is actually shown is the existence of neighboring configurations with the

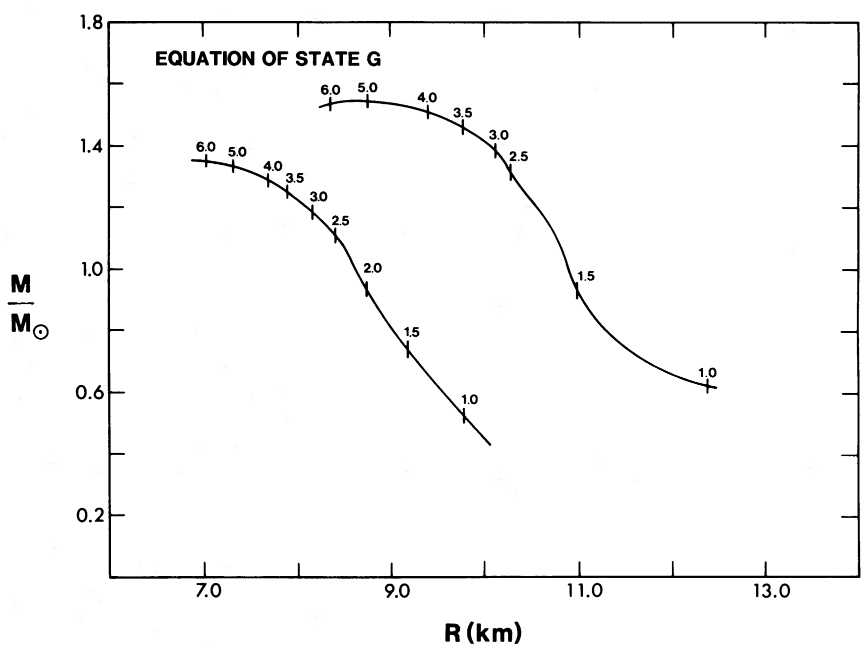

FIG. 7.—Gravitational mass vs. equatorial radius as in Figs. 5 and 6, for models based on EOS G

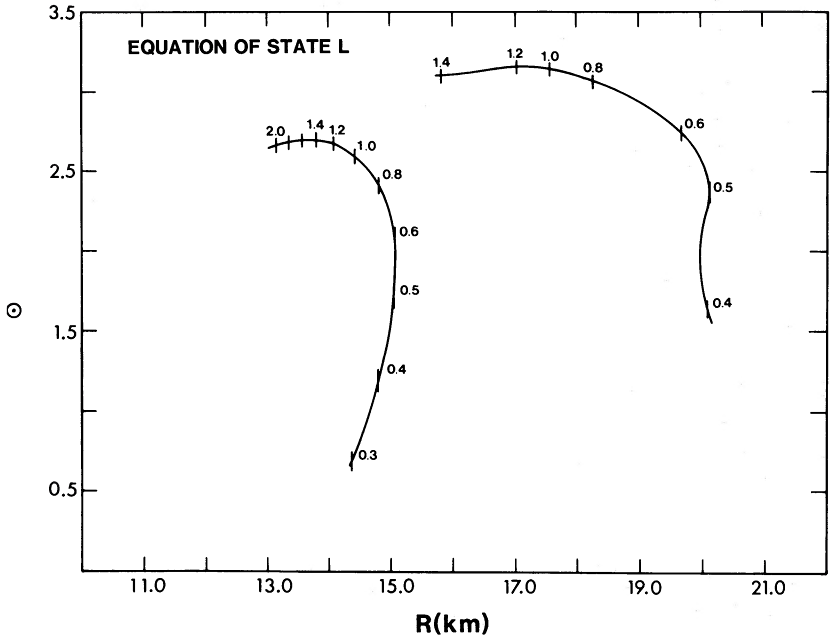

FIG. 8.—Gravitational mass vs. equatorial radius as in Figs. 5–7, for models based on EOS L(MF)

same baryon number and total angular momentum, but with lower energy. Because these lower energy configurations need not be accessible to perturbations that conserve the angular momentum of each fluid element, the instability may be secular: that is, it may proceed on the time scale corresponding to viscous redistribution of the star's angular momentum. This growth time is in any event short enough that observed neutron stars will be secularly stable against collapse.

An interesting consequence follows from the fact that instability to collapse sets in at or before the upper mass limit: For a given EOS, the model with maximum mass and baryon number also has the largest red- and blueshifts, the largest value of the frame-dragging frequency, and the greatest frequency of rotation (and equatorial velocity) among all uniformly rotating configurations that are stable against collapse. Because the stiffness of a given EOS increases with increasing density, the parameter t also appears to be greatest for the maximum mass configuration.

b) *Maximum Red- and Blueshifts*

In nearly Newtonian stars at termination point, shifts in spectral line frequency are dominated by the Doppler shift, because the gravitational redshift is higher order in v/c. If z_B (z_F) denotes the frequency shift of backward (forward) photons emitted at the equator, we have

$$\left.\begin{matrix} z_B \\ z_F \end{matrix}\right\} = \pm \frac{v}{c} \, .$$

In neutron stars, however, the gravitational redshift plays a much larger role. In terms of the metric (1), the frequency shifts have the form

$$\left.\begin{matrix} z_B \\ z_F \end{matrix}\right\} = \left(1 \pm \frac{\omega}{c} e^{\psi - \nu}\right)^{-1} \left(\frac{1 \pm v/c}{1 \mp v/c}\right) - 1 \, ,$$

and for the maximum-mass models of Table 2, we have $|z_B/z_F| \approx 6$.

The large magnitude of the shifts reflects large increases in radius for stars with Ω near Ω_K. There is little difference in the maximum red- and blueshifts as the compressibility changes. One might have expected that the stiffer stars, with larger radii, would have correspondingly larger values of v_{eq} and thus larger frequency shifts. However, the limiting frequency Ω_K is smaller in the stiff models, and the net result is that maximum values of v_{eq}/c and of the frequency shifts are insensitive to compressibility.

c) *Maximum Moments of Inertia*

As is the case for spherical neutron stars, the model with maximum moment of inertia for a given EOS has a substantially lower central density than does the maximum mass model. The reason is, of course, that models with lower densities have much larger radii. The large increase in radius produced by rotation implies that the moment of inertia increases much more than does the maximum mass. The effect of rotation on the moment of inertia I is shown in Figure 9, for models based on EOS, C, F, G, and L. As usual, the effect of rotation is greatest on the stiffest models, with I changing by over 70%, but even for the centrally condensed models of EOS G, we find a 60% increase over the maximum value along the spherical sequence.

As we discuss in § V, however, a sparse envelope of the star accounts for the large change in radius. The structure of the star, as reflected by the distribution of its mass and by the gravitational potentials (the metric) changes less. As a result, the moment of inertia does not mirror the change in the quantity MR^2 caused by rotation: I/MR^2 decreases with increasing rotation, for fixed mass or fixed polar redshift. In spherical relativistic models I/MR^2 is substantially larger than in Newtonian configurations with comparable stiffness (Chandrasekhar and Miller 1974): in fact, for all EOSs, we find that I/MR^2 exceeds the maximum Newtonian value ($\frac{2}{5}$) when $\beta < 0.5$ ($R < 4GM/c^2$). Even for rapid rotation ($\Omega \approx \Omega_K$), $I/MR^2 > \frac{2}{5}$ for EOS L. But for more compressible models with

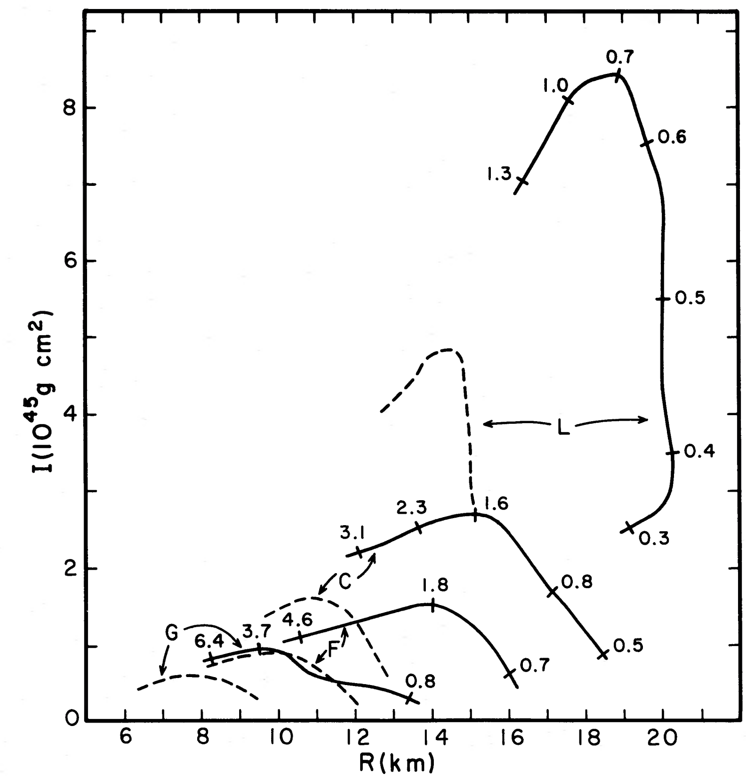

FIG. 9.—Moment of inertia vs. equatorial radius for sequences of models based on EOSs C(BJ I), F, G, and L(MF). For each EOS a sequence of spherical models is represented by a dashed line, while a solid line represents models rotating at maximum (Keplerian) angular velocity, $\Omega = \Omega_K$. Along each curve with $\Omega = \Omega_K$ tickmarks are labeled with the value of the model's central density in units of 10^{15} g cm^{-3}.

$\Omega \approx \Omega_K$, and with I near I_{max}, the effect is muted: the rotating models are less relativistic and I/MR^2 is smaller (by up to 25%) than for the corresponding spherical model.

d) *Sequences of Stellar Models*

In addition to the $M_0 \approx 1.4\ M_\odot$ sequences discussed in § III, families of stars with several values of the injection energy β were constructed for each of the equations of state C(BJ I), FP, G, L(MF), and N*(RMF). Along each sequence β is fixed, while the angular velocity runs from zero to the Kepler frequency Ω_K, and each sequence includes a model with frequency equal to that of the millisecond (fast) pulsar 1937+214 ($\Omega_{fp} = 0.4033 \times 10^4$ s^{-1}). Quantities characterizing the models are listed in Tables 3–7.

In Figures 10–15 potentials are plotted along a radial direction in the equatorial plane for representative models from EOS G (softest), C(BJ I) (intermediate), and L(MF) (stiffest).

For low-density models, rotation has little effect on the potentials, reflecting the fact that the sequences terminate at small values of rotation, measured by the dimensionless parameter t, or by $\Omega^2/\pi G\epsilon_c$. As the central density increases, the value of t at termination increases (as mentioned earlier,

TABLE 3

SEQUENCES OF MODELS FOR EQUATION OF STATE

β	Ω	ϵ_c (10^{15} g cm^{-3})	$M/M_\odot$	$M_0/M_\odot$	R	ω_c/Ω	T/W	V_{eq}/c	I (10^{45} g cm^2)	cJ/GM^2	e	Z_p	Z_B	Z_F
0.446.........	0	3.06	1.85	2.14	9.8	0.74	0	0	...	0	0	0.50	0.50	+0.50
	0.300	2.93	1.86	2.15	9.9	0.74	0.007	0.10	1.56	0.12	0.15	0.50	0.74	+0.29
	0.403	2.77	1.88	2.16	10.3	0.74	0.012	0.14	1.63	0.16	0.26	0.50	0.81	+0.20
	0.720	2.12	1.94	2.22	11.6	0.69	0.052	0.27	2.01	0.33	0.50	0.50	1.13	−0.06
	0.869	1.58	2.03	2.29	15.0	0.66	0.110	0.43	2.68	0.50	0.72	0.50	1.41	−0.30
0.676.........	0	1.00	1.32	1.44	12.1	0.43	0	0	...	0	0	0.22	0.22	+0.22
	0.150	0.98	1.32	1.43	12.3	0.43	0.004	0.06	1.28	0.11	0.13	0.21	0.31	+0.13
	0.300	0.95	1.31	1.42	12.5	0.42	0.017	0.13	1.32	0.22	0.27	0.22	0.40	+0.04
	0.403	0.91	1.30	1.41	13.3	0.42	0.034	0.18	1.38	0.32	0.47	0.22	0.48	−0.03
	0.570	0.77	1.29	1.39	16.9	0.40	0.093	0.32	1.69	0.57	0.74	0.22	0.67	−0.22
0.811.........	0	0.60	0.81	0.85	13.1	0.26	0	0	...	0	0	0.11	0.11	+0.11
	0.150	0.59	0.81	0.84	12.9	0.26	0.007	0.07	0.72	0.17	0.25	0.11	0.19	+0.03
	0.300	0.56	0.80	0.83	14.0	0.26	0.030	0.14	0.77	0.38	0.47	0.11	0.28	−0.06
	0.360	0.54	0.79	0.82	14.8	0.25	0.048	0.18	0.81	0.49	0.60	0.11	0.33	−0.10
	0.410	0.51	0.78	0.81	18.1	0.25	0.071	0.25	0.87	0.62	0.71	0.11	0.38	−0.16

TABLE 4

SEQUENCES OF MODELS FOR EQUATION OF STATE FP

β	Ω	ϵ_c (10^{15} g cm^{-3})	$M/M_\odot$	$M_0/M_\odot$	R	ω_c/Ω	T/W	V_{eq}/c	I (10^{45} g cm^2)	cJ/GM^2	e	Z_p	Z_B	Z_F
0.376.........	0	3.03	1.94	2.33	9.2	0.80	0	0	...	0	0	0.63	0.64	+0.64
	0.150	3.01	1.95	2.34	9.2	0.80	0.001	0.05	1.61	0.05	...	0.63	0.76	+0.52
	0.403	2.80	1.96	2.36	9.5	0.79	0.011	0.13	1.68	0.14	0.17	0.63	0.99	+0.32
	0.600	2.57	1.98	2.37	9.7	0.78	0.025	0.19	1.77	0.21	0.32	0.63	1.19	+0.17
	0.960	1.96	2.04	2.40	11.3	0.73	0.090	0.36	2.19	0.42	0.49	0.63	1.64	−0.15
	1.038	1.73	2.10	2.44	13.1	0.71	0.131	0.39	2.58	0.51	0.60	0.63	1.80	−0.30
0.629.........	0	1.28	1.32	1.46	10.3	0.47	0	0	...	0	0	0.26	0.26	+0.26
	0.150	1.26	1.32	1.47	10.6	0.47	0.003	0.05	1.09	0.09	0.22	0.26	0.35	+0.18
	0.403	1.21	1.31	1.44	11.1	0.46	0.024	0.15	1.14	0.25	0.30	0.26	0.50	+0.03
	0.600	1.08	1.30	1.42	12.0	0.45	0.066	0.24	1.29	0.43	0.54	0.26	0.64	−0.10
	0.696	0.93	1.30	1.41	13.7	0.44	0.113	0.32	1.53	0.60	0.73	0.26	0.76	−0.21
	0.705	0.92	1.30	1.41	14.9	0.43	0.120	0.35	1.56	0.63	0.77	0.26	0.80	−0.24
0.777.........	0	0.77	0.81	0.85	10.7	0.29	0	0	...	0	0	0.13	0.13	+0.13
	0.150	0.77	0.80	0.85	10.8	0.29	0.005	0.05	0.58	0.14	0.12	0.13	0.20	+0.06
	0.300	0.73	0.79	0.84	11.2	0.28	0.022	0.11	0.61	0.29	0.34	0.13	0.28	−0.01
	0.403	0.69	0.78	0.83	11.7	0.28	0.043	0.16	0.64	0.43	0.51	0.14	0.34	−0.10
	0.480	0.66	0.77	0.81	12.5	0.27	0.068	0.20	0.68	0.56	0.62	0.14	0.39	−0.11
	0.540	0.63	0.77	0.80	14.7	0.27	0.101	0.26	0.75	0.71	0.72	0.14	0.47	−0.19
	0.542	0.63	0.77	0.80	15.1	0.27	0.102	0.27	0.75	0.72	0.72	0.14	0.48	−0.19

TABLE 5

SEQUENCES OF MODELS FOR EQUATION OF STATE G

β	Ω	ϵ_c (10^{15} g cm^{-3})	$M/M_\odot$	$M_0/M_\odot$	R	ω_c/Ω	T/W	V_{eq}/c	I (10^{45} g cm^2)	cJ/GM^2	e	Z_p	Z_B	Z_F
0.531.........	0.30	3.46	1.26	1.40	7.7	0.63	0.005	0.09	0.622	0.13	0.16	0.37	0.56	+0.26
	0.54	3.28	1.26	1.40	7.9	0.62	0.016	0.16	0.649	0.25	0.33	0.37	0.69	+0.13
	0.72	3.10	1.27	1.41	8.2	0.61	0.032	0.22	0.688	0.35	0.46	0.37	0.80	+0.04
	0.87	2.84	1.27	1.41	8.9	0.60	0.053	0.30	0.748	0.45	0.57	0.37	0.89	−0.06
	0.96	2.65	1.28	1.42	9.4	0.59	0.072	0.35	0.813	0.53	0.61	0.37	0.97	−0.13
	0.99	2.55	1.29	1.42	9.7	0.59	0.081	0.37	0.849	0.57	0.64	0.37	1.00	−0.16
	1.01	2.51	1.29	1.43	10.4	0.58	0.086	0.40	0.872	0.59	0.67	0.37	1.02	−0.20
0.844.........	0	0.97	0.53	0.55	8.4	0.23	0	0	0.259	0	0	0.09	0.09	+0.09
	0.15	0.95	0.53	0.55	9.0	0.23	0.004	0.05	0.262	0.16	0.14	0.09	0.15	+0.04
	0.36	0.88	0.52	0.53	10.3	0.22	0.026	0.13	0.278	0.42	0.51	0.09	0.24	−0.05
	0.45	0.80	0.51	0.53	11.9	0.22	0.045	0.20	0.294	0.56	0.65	0.09	0.30	−0.12
	0.47	0.79	0.51	0.52	13.3	0.22	0.051	0.23	0.299	0.61	0.73	0.09	0.34	−0.15

TABLE 6

SEQUENCES OF MODELS FOR EQUATION OF STATE L(MF)

β	Ω	ϵ_c (10^{15} g cm^{-3})	$M/M_\odot$	$M_0/M_\odot$	R	ω_c/Ω	T/W	V_{eq}/c	I (10^{45} g cm^2)	cJ/GM^2	e	Z_p	Z_B	Z_F
0.467.........	0	1.10	2.60	3.07	14.2	0.69	0	0	4.79	0	0	0.46	0.46	+0.46
	0.300	0.99	2.64	3.11	14.7	0.68	0.017	0.17	5.18	0.25	0.31	0.46	0.80	+0.16
	0.450	0.85	2.66	3.13	15.7	0.66	0.043	0.27	5.75	0.41	0.48	0.46	1.00	0.00
	0.540	0.71	2.70	3.15	16.8	0.64	0.073	0.38	6.52	0.55	0.60	0.46	1.16	−0.12
	0.585	0.64	2.78	3.21	18.0	0.62	0.100	0.40	7.41	0.64	0.68	0.46	1.26	−0.20
	0.600	0.61	2.81	3.23	19.8	0.61	0.114	0.45	7.88	0.68	0.72	0.46	1.31	−0.25
0.620.........	0	0.55	2.00	2.26	15.2	0.48	0	0	3.71	0	0	0.27	0.27	+0.27
	0.300	0.51	1.97	2.22	15.9	0.47	0.027	0.17	3.90	0.34	0.41	0.27	0.54	+0.02
	0.360	0.50	1.96	2.19	16.1	0.46	0.041	0.21	4.04	0.43	0.50	0.27	0.60	−0.04
	0.420	0.48	1.95	2.16	16.7	0.46	0.062	0.26	4.23	0.53	0.60	0.27	0.67	−0.09
	0.450	0.46	1.95	2.15	17.4	0.45	0.075	0.30	4.42	0.60	0.65	0.27	0.71	−0.14
	0.488	0.44	1.94	2.13	19.8	0.45	0.100	0.32	4.78	0.71	0.74	0.27	0.79	−0.22
0.756.........	0	0.40	1.30	1.41	14.7	0.32	0	0	2.07	0	0	0.15	0.15	+0.15
	0.300	0.35	1.26	1.36	15.9	0.31	0.038	0.18	2.28	0.49	0.54	0.15	0.38	−0.07
	0.360	0.33	1.24	1.33	18.2	0.30	0.063	0.24	2.44	0.65	0.67	0.15	0.45	−0.14
	0.375	0.32	1.24	1.32	18.5	0.30	0.072	0.26	2.50	0.70	0.71	0.15	0.47	−0.16
	0.383	0.31	1.23	1.32	19.1	0.30	0.076	0.27	2.53	0.73	0.74	0.15	0.49	−0.18

TABLE 7

SEQUENCES OF MODELS FOR EQUATION OF STATE N*(RMF)

β	Ω	ϵ_c (10^{15} g cm^{-3})	$M/M_\odot$	$M_0/M_\odot$	R	ω_c/Ω	T/W	V_{eq}/c	I (10^{45} g cm^2)	cJ/GM^2	e	Z_p	Z_B	Z_F
0.960.........	0	0.253	0.215	0.216	15.9	...	0	0	0.120	0	0	0.020	0.021	+0.021
	0.060	0.252	0.214	0.215	16.4	0.083	0.002	0.032	0.120	0.18	0.21	0.020	0.055	−0.014
	0.090	0.252	0.214	0.215	17.0	0.083	0.005	0.049	0.121	0.27	0.31	0.020	0.074	−0.033
	0.120	0.250	0.213	0.214	18.2	0.082	0.010	0.068	0.122	0.36	0.48	0.020	0.096	−0.055
	0.135	0.250	0.212	0.213	19.5	0.082	0.012	0.082	0.123	0.41	0.57	0.020	0.111	−0.070
	0.147	0.249	0.212	0.213	22.7	0.082	0.015	0.112	0.124	0.45	0.71	0.021	0.136	−0.095
0.715.........	0	0.50	1.33	1.44	13.8	...	0	0	1.74	0	0	0.18	0.18	+0.18
	0.150	0.50	1.32	1.43	14.0	0.35	0.006	0.070	1.74	0.14	0.15	0.18	0.28	+0.08
	0.300	0.48	1.30	1.40	14.5	0.35	0.030	0.145	1.79	0.31	0.40	0.18	0.39	−0.015
	0.403	0.46	1.27	1.36	15.4	0.34	0.060	0.207	1.88	0.46	0.60	0.18	0.47	−0.095
	0.480	0.43	1.25	1.33	18.0	0.34	0.098	0.289	2.03	0.62	0.73	0.18	0.57	−0.195
	0.482	0.43	1.25	1.33	18.4	0.34	0.099	0.295	2.04	0.63	0.74	0.19	0.58	−0.203
0.374.........	0	2.09	2.60	3.12	12.2	...	0	0	...	0	0	0.64	0.65	+0.65
	0.150	1.98	2.63	3.16	12.5	0.81	0.002	0.062	3.98	0.067	0.04	0.64	0.80	+0.47
	0.300	1.82	2.66	3.19	12.6	0.80	0.011	0.126	4.15	0.14	0.11	0.64	1.01	+0.33
	0.403	1.61	2.69	3.23	13.0	0.78	0.021	0.175	4.43	0.19	0.26	0.64	1.16	+0.22
	0.600	1.20	2.78	3.31	14.4	0.75	0.059	0.288	5.23	0.33	0.45	0.64	1.46	−0.02
	0.729	0.93	2.87	3.37	16.2	0.71	0.110	0.389	6.35	0.46	0.63	0.64	1.72	−0.19
	0.755	0.83	2.91	3.38	18.5	0.70	0.014	0.467	7.13	0.53	0.72	0.64	1.83	−0.31

this is due to the fact that all EOSs considered are stiffer at higher densities). Rotation thus has a somewhat greater effect. For the highest density models (with smallest values of the injection energy β), there is no corresponding spherical model with the same rest mass.

The shapes of stellar surfaces are illustrated by embedding diagrams in Figures 16*a*–20*a* for sequences again based on EOSs G, C(BJ I) and L(MF). In the adjacent figures (Figs. 16*b*–20*b*), density profiles are plotted for the corresponding stellar models. An additional set of density profiles in Figure 21 illustrate sharp differences in the structure of stars at $\Omega \approx \Omega_K$, as the EOS is varied at fixed baryon mass.

Tables 8–11 describe sequences of stars with $\Omega \approx \Omega_K$ for EOSs C(BJ I), F, G, and L(MF).

The numerical code converged for models up to $\Omega = \Omega_K$. In fact, because the effect of our finite grid is similar to enclosing the star in a finite spherical box, models with $\Omega > \Omega_K$ often converged as well. In these $\Omega > \Omega_K$ models, the density in the

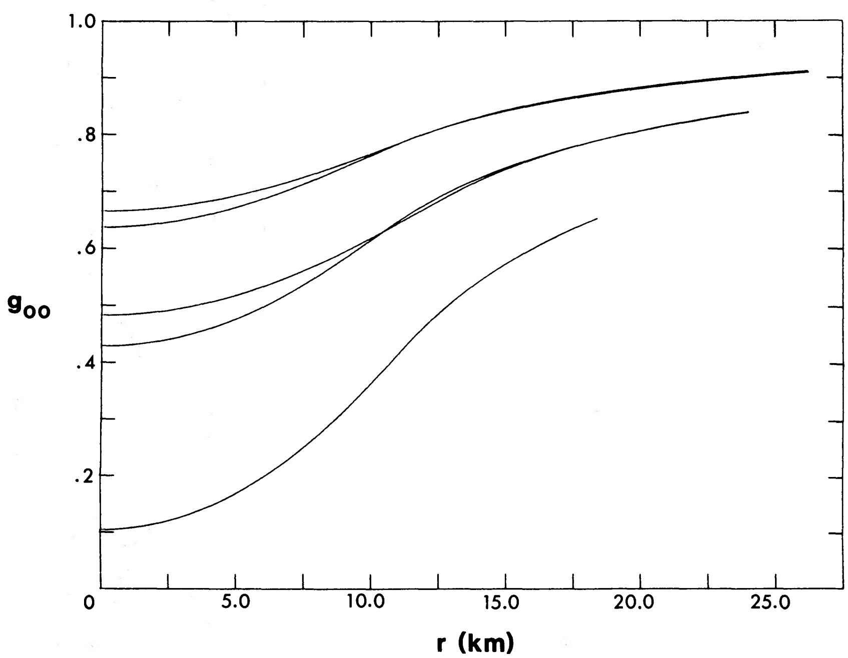

FIG. 10.—For five models based on EOS C(BJ I), the metric component $-g_{00} = -t^a t_a$ vs. the radial coordinate r for which $2\pi r$ is the circumference of a circle of radius r in the equatorial plane. The top pair of curves describe models with the same injection energy, $\beta = 0.811$ (and with $M_0 \approx 0.8\ M_\odot$); the lower curve of the pair represents a nearly spherical star, the upper curve a model rotating at $\Omega \approx \Omega_K$ ($\Omega = 0.41 \times 10^4\ s^{-1}$). The middle pair of curves correspond to models with $\beta = 0.676$ ($M_0 \approx 1.4\ M_\odot$), with the lower curve (at $r = 0$) representing a nearly spherical model, and the upper (at $r = 0$) a model rotating at $\Omega \approx \Omega_K$ ($\Omega = 0.57 \times 10^4\ s^{-1}$). The single (lowest) curve represents a model with $\beta = 0.352$, $M_0 = 2.47\ M_\odot$, and $\Omega \approx \Omega_K$; there is no corresponding spherical model because the mass (and rest mass) exceed the limits for spherical models based on EOS C. Properties of these models are listed in Tables 2 and 8.

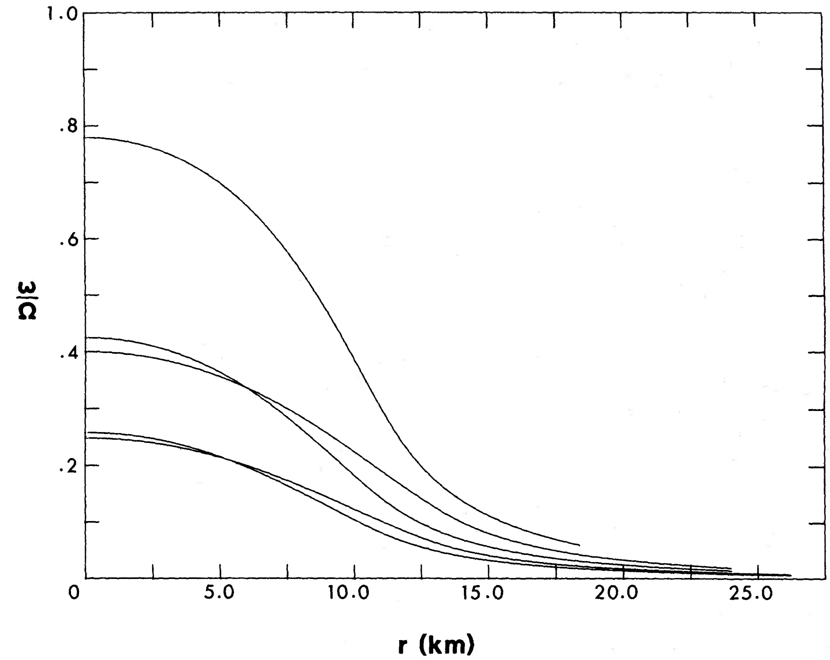

FIG. 11.—For the five models of Fig. 10 (EOS C), the ratio ω/Ω of the frame dragging parameter to the model's angular velocity vs. the radial coordinate r. ($\omega = -\phi^a t_a/\phi^b \phi_b$ is the angular velocity of a zero angular momentum observer.) The order of the curves is the reverse of that in Fig. 10: From top to bottom at $r = 0$, the curves correspond to models with $\beta = 0.352, \Omega \approx \Omega_K$; $\beta = 0.676, \Omega \approx 0$ and $\Omega \approx \Omega_K$; $\beta = 0.811, \Omega \approx 0$ and $\Omega \approx \Omega_K$.

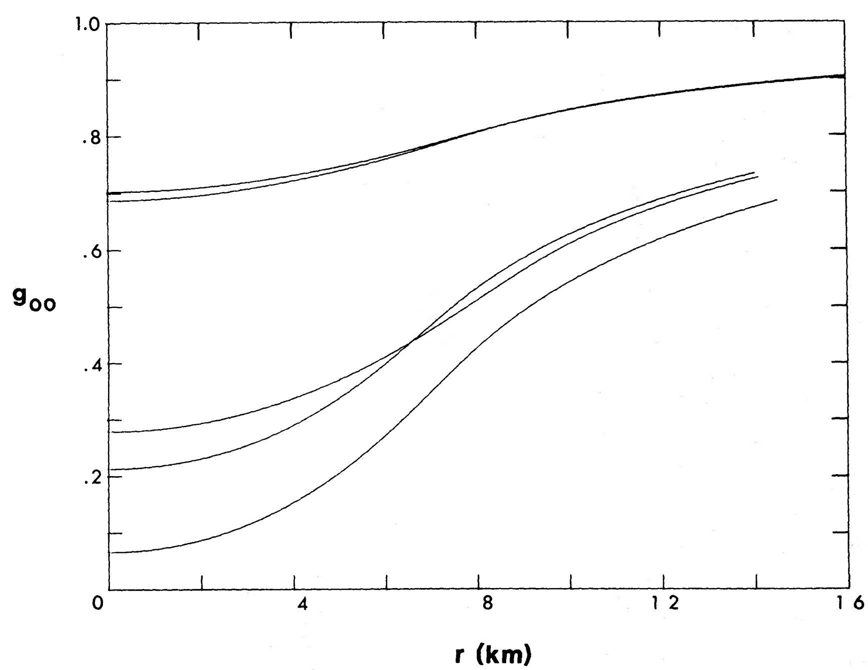

FIG. 12.—For five models based on EOS G, the metric component g_{00} vs. the radial coordinate r, as in Fig. 10. The top pair of curves describe models with $\beta = 0.844$ ($M_0 \approx 0.53\ M_\odot$); the upper curve of the pair represents a nearly spherical model, the lower curve a model with $\Omega \approx \Omega_K$ ($\Omega = 0.47 \times 10^{15}$ g cm^{-3}). For the middle pair, $\beta = 0.531$ ($M_0 \approx 1.4\ M_\odot$); and $\Omega \approx 0$ for the lower curve at $r = 0$, $\Omega \approx \Omega_K$ ($\Omega = 1.01 \times 10^4$ s^{-1}) for the upper. For the single lowest curve, $\beta = 0.32$ ($M_0 = 1.71\ M_\odot$) and $\Omega \approx \Omega_K$ ($\Omega = 1.61 \times 10^{15}$ g cm^{-3}); again there is no corresponding spherical model with mass (or rest mass) as large as this. Properties of these models are listed in Tables 5 and 10.

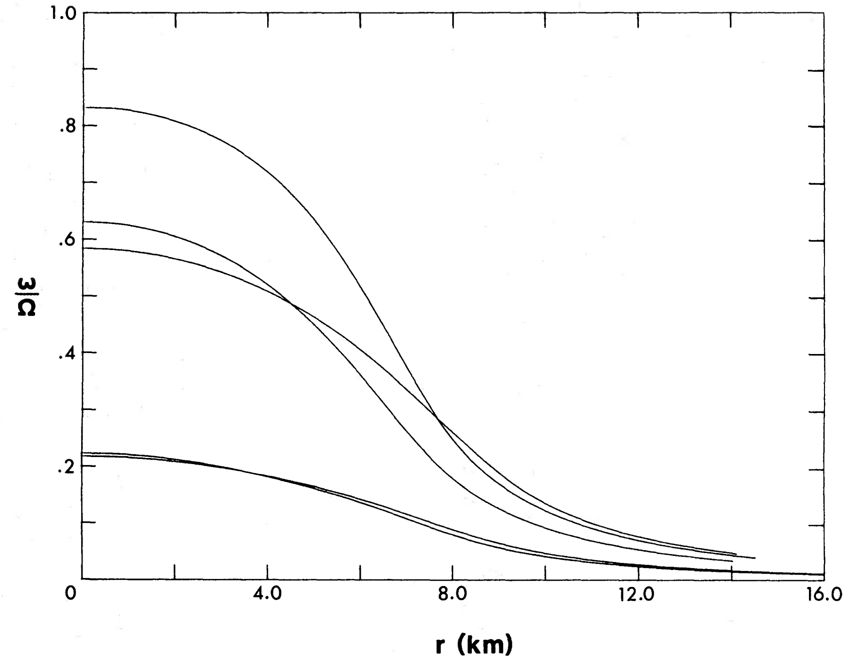

FIG. 13.—For the five models of Fig. 12 (EOS G), the ratio ω/Ω of the frame dragging parameter to the model's angular velocity vs. the radial coordinate r. The order of the curves is the reverse of that in Fig. 12: From top to bottom at $r = 0$, the curves correspond to models with $\beta = 0.32, \Omega \approx \Omega_K$; $\beta = 0.531$, $\Omega \approx 0$ and $\Omega \approx \Omega_K$; $\beta = 0.844, \Omega \approx 0$ and $\Omega \approx \Omega_K$.

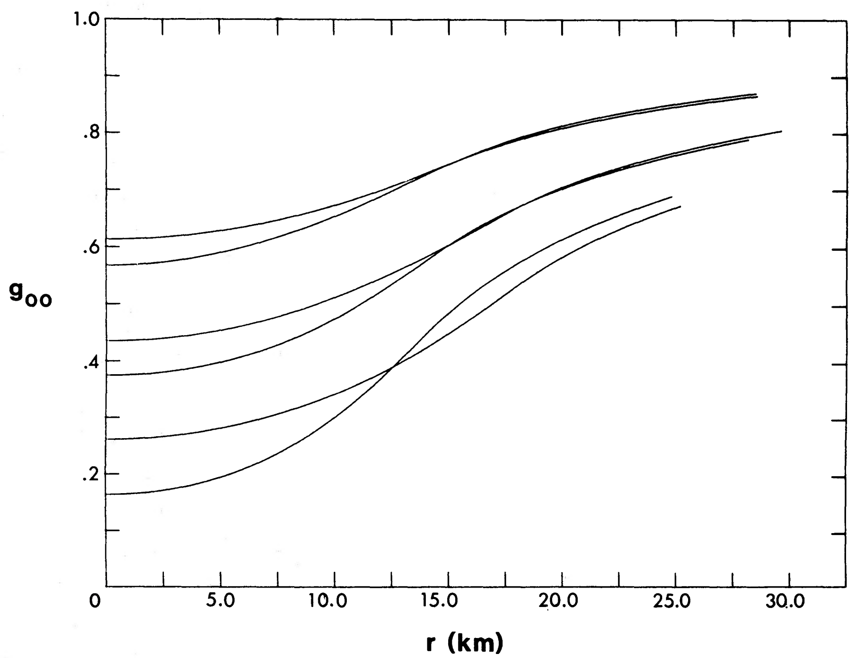

FIG. 14.—For six models based on EOS L(MF), the metric component g_{00} is plotted against the radial coordinate r, as in Figs. 10 and 11. The top pair of curves describe models with $\beta = 0.756$ ($M_0 \approx 1.4\ M_\odot$); for the middle pair, $\beta = 0.62$ ($M_0 \approx 2.2\ M_\odot$); and for the lowest pair $\beta = 0.467$ ($M_0 \approx 3.1\ M_\odot$). The upper curve (at $r = 0$) of each pair represents a nearly spherical model, the lower curve a model with $\Omega \approx \Omega_K$ ($\Omega = 0.38 \times 10^4\ \mathrm{s}^{-1}$, $\Omega = 0.49 \times 10^4\ \mathrm{s}^{-1}$, $\Omega = 0.60 \times 10^4\ \mathrm{s}^{-1}$, respectively for the $\beta = 0.756$, 0.62, and 0.467 models). Properties of these models are listed in Table 6.

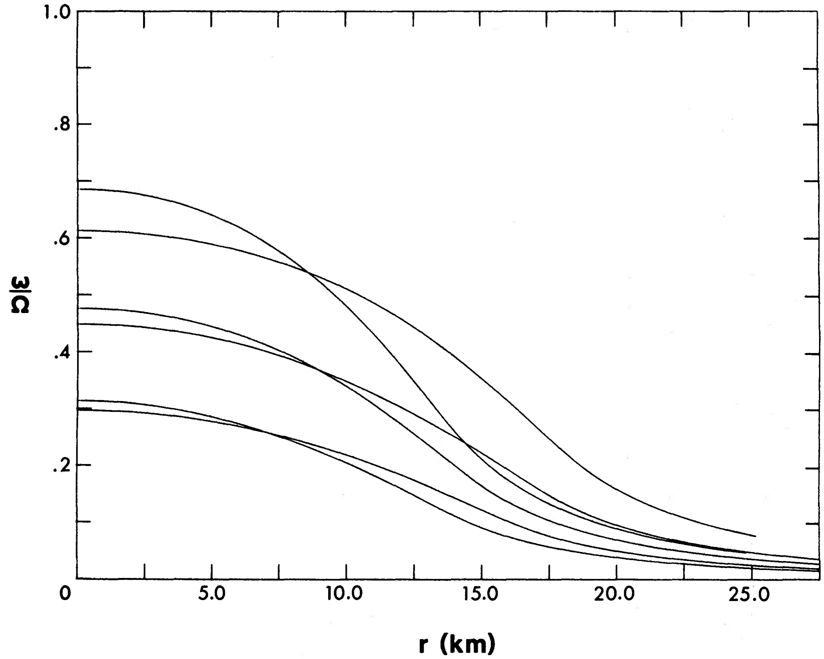

FIG. 15.—For the six models of Fig. 14 [EOS L(MF)], the ratio ω/Ω of the frame dragging parameter to the model's angular velocity vs. the radial coordinate r. The order of the curves is the reverse of that in Fig. 14: From top to bottom at $r = 0$, the curves correspond to models with $\beta = 0.467$, $\Omega = 0$ and $\Omega \approx \Omega_K$; $\beta = 0.62$, $\Omega \approx 0$ and $\Omega \approx \Omega_K$; $\beta = 0.756$, $\Omega \approx 0$ and $\Omega \approx \Omega_K$.

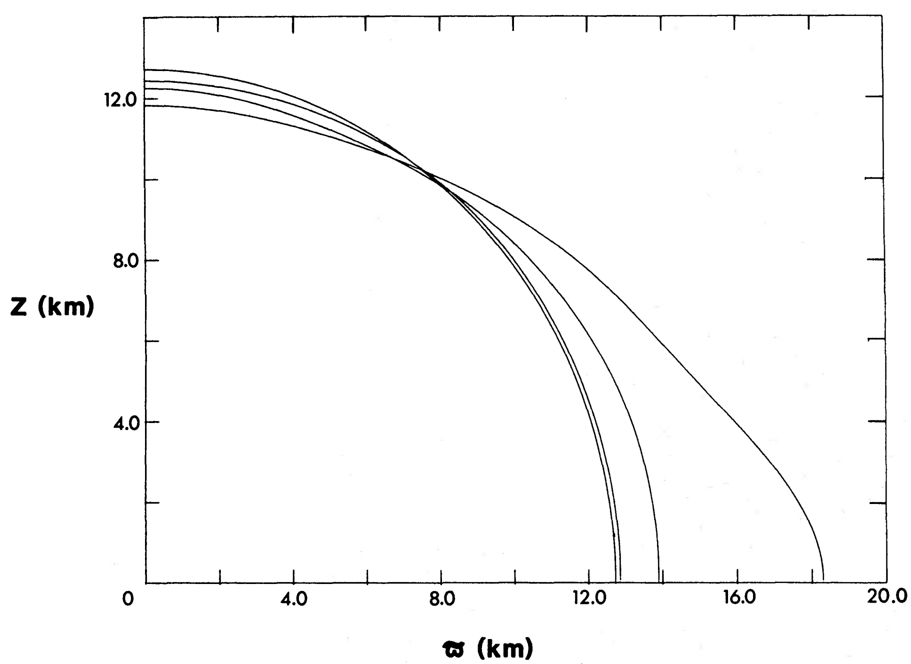

FIG. 16.—The surfaces of four models based on EOS C(BJ I) are depicted here by four embedding diagrams. Surfaces of revolution obtained by sweeping the curves about the z-axis have the intrinsic geometry of the stellar surfaces. The four models have injection energy $\beta = 0.811$, rest mass $M_0 = 0.8\ M_\odot$, and angular velocities $\Omega = 0, 0.15 \times 10^4\ s^{-1}, 0.30 \times 10^4\ s^{-1}$, and $0.41 \times 10^4\ s^{-1} \approx \Omega_K$. The increase in equatorial radius (the value of ϖ at $z = 0$) with increasing angular velocity may be used to identify the curves.

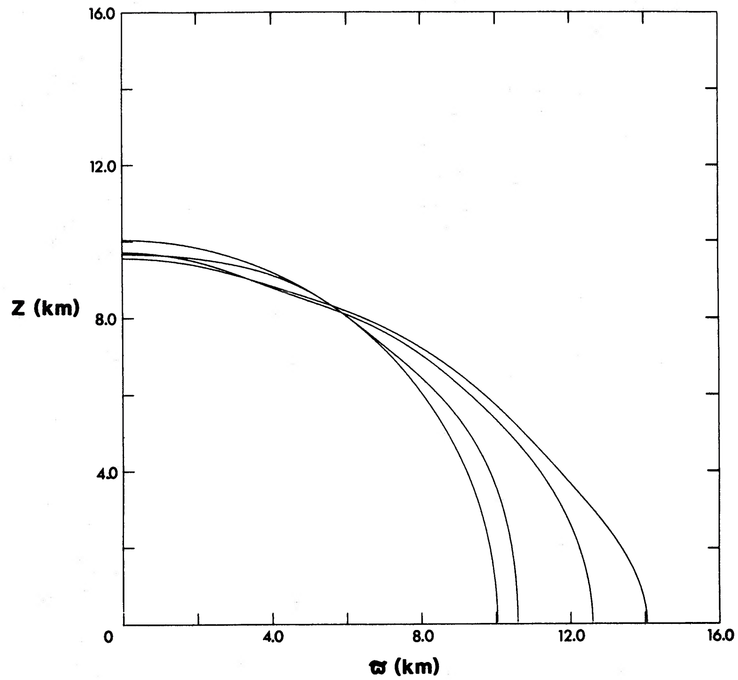

FIG. 17a

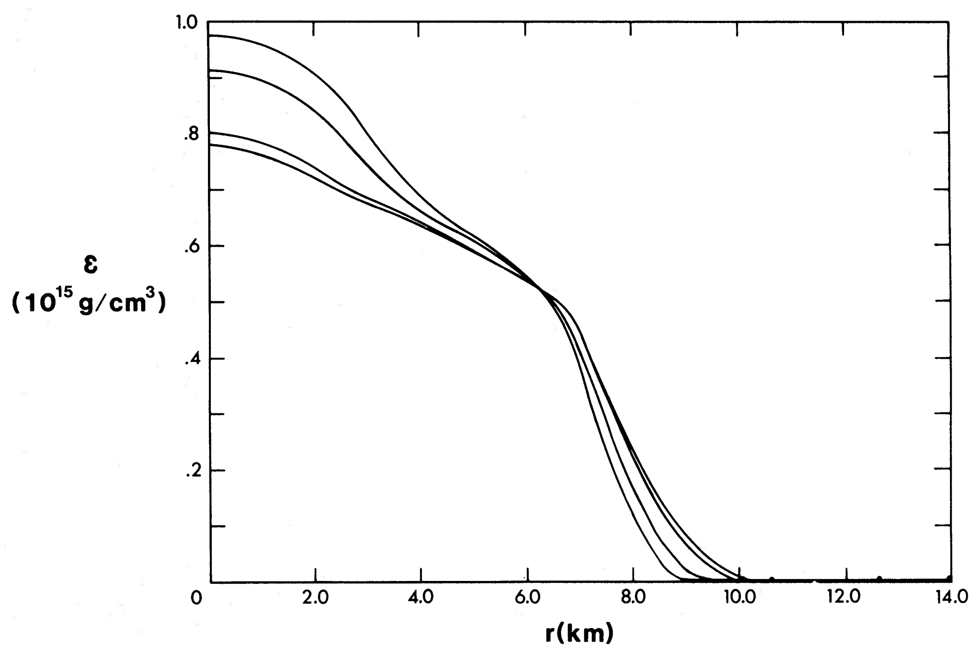

FIG. 17b

FIG. 17.—(a) The surfaces of four models based on EOS G depicted by embedding diagrams as in Fig. 16. For these models $\beta = 0.844$ ($M_0 \approx 0.53\ M_\odot$); and $\Omega = 0, 0.30 \times 10^4\ \mathrm{s}^{-1}, 0.45 \times 10^4\ \mathrm{s}^{-1}$, and $0.47 \times 10^4\ \mathrm{s}^{-1} \approx \Omega_K$. ($b$) For the four models of (a), the energy density in the equatorial plane vs. the radial coordinate r. Curves may be identified by the decrease in central density (or by the increase in radius) with increasing angular velocity. The location of each stellar surface is indicated by a dot along the r-axis, marking the end of the $\epsilon(r)$ curve for that model.

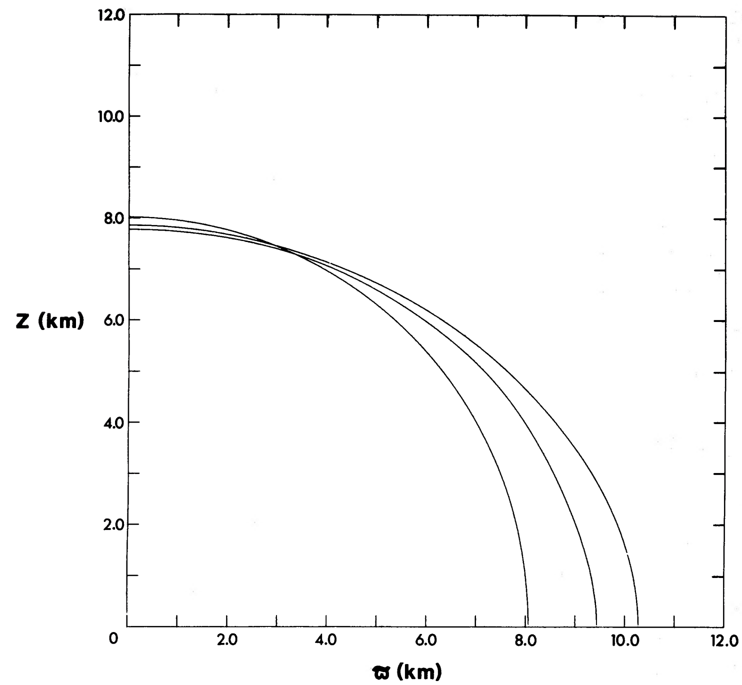

FIG. 18*a*

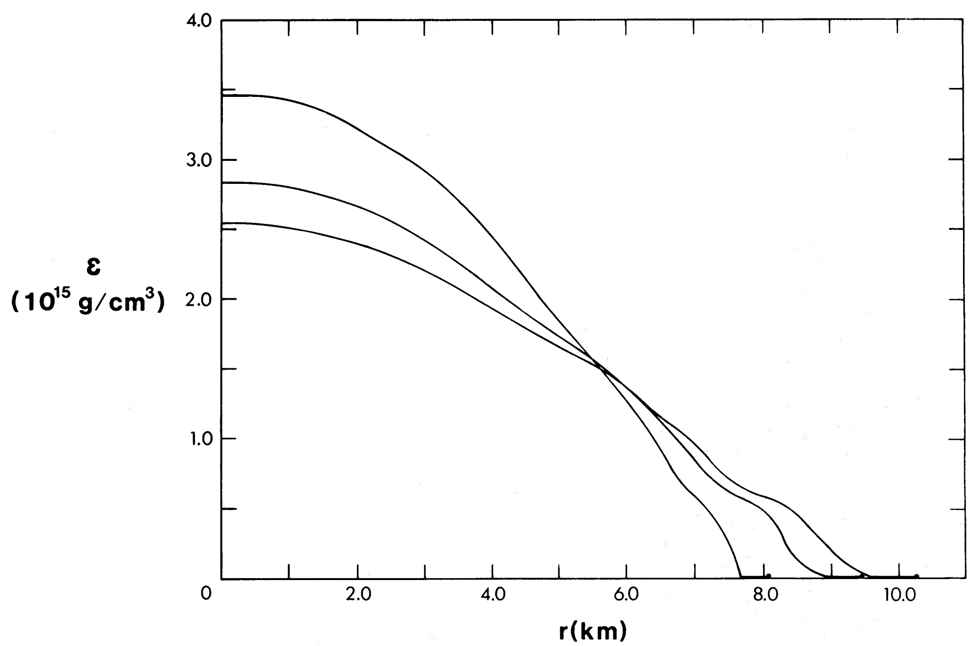

FIG. 18*b*

FIG. 18.—(*a*) The surfaces of three additional models based on EOS G depicted by embedding diagrams as in Fig. 16. For these models $\beta = 0.531$ ($M_0 \approx 1.4$ $M_\odot$); and $\Omega = 0.15 \times 10^4$ s^{-1}, 0.54×10^4 s^{-1}, and 0.99×10^4 s$^{-1} \approx \Omega_K$. (*b*) For the three models of (*a*), the energy density in the equatorial plane vs. the radial coordinate *r*, as in Fig. 17*b*.

equatorial plane reaches a minimum value at a radius slightly larger than that of the Ω_K model and then rises again until the edge of the grid is reached. The Keplerian frequency can also be found numerically using equations (23a)–(23b). With Ω_K carefully determined as the smallest value of Ω for which the density first reaches the edge of the grid, the result agrees with that obtained from equation (23) to 2%–4%. The error presumably reflects our inaccuracy in locating the stellar surface between radial grid points.

V. ASTROPHYSICAL IMPLICATIONS

a) Growth Times for Nonaxisymmetric Instability

As noted previously, because sequences of uniformly rotating neutron stars appear to end prior to an $m = 2$ (bar mode) instability, modes with angular dependence exp $(im\phi)$ for $m = 3$ and $m = 4$ are expected to set the upper limit on rotation for accreting neutron stars with weak magnetic fields. We can use our models to estimate the growth rates of these

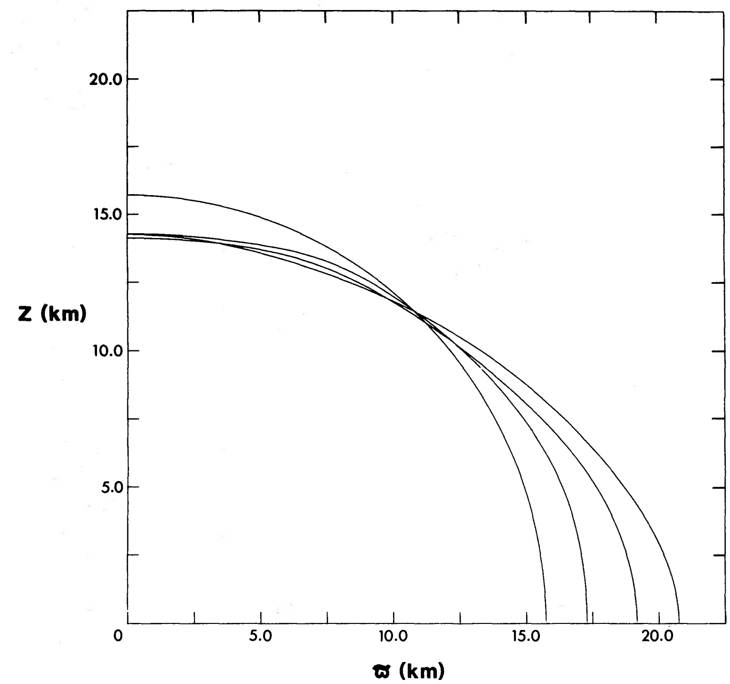

FIG. 19a

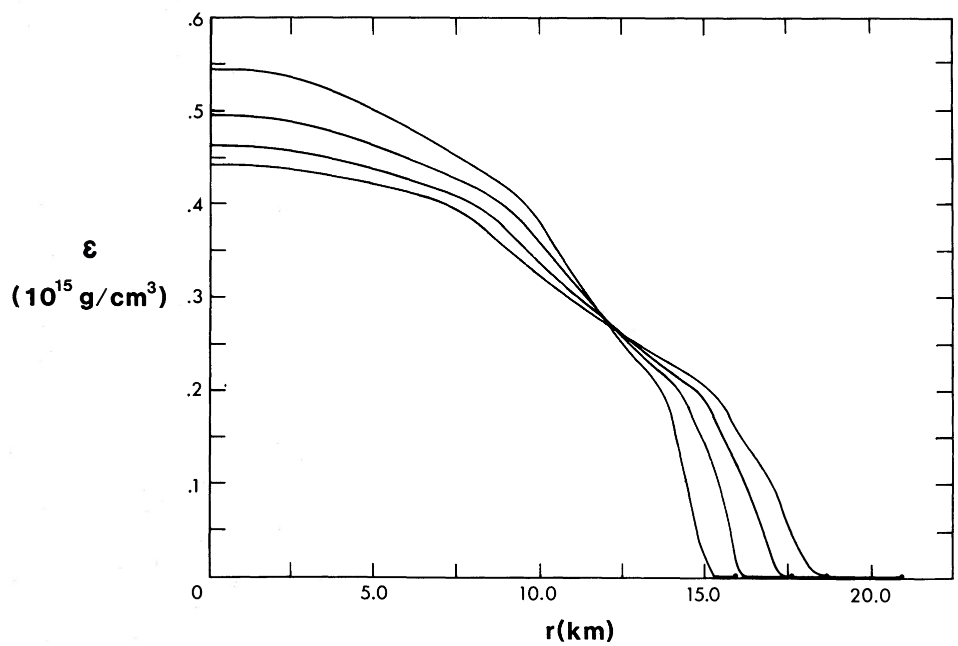

FIG. 19b

FIG. 19.—(a) The surfaces of four models based on EOS L(MF) depicted by embedding diagrams as in Fig. 16. For these models $\beta = 0.756$ ($M_0 \approx 1.4\ M_\odot$); and $\Omega = 0, 0.30 \times 10^4\ s^{-1}, 0.36 \times 10^4\ s^{-1}$, and $0.383 \times 10^4\ s^{-1} \approx \Omega_K$. (b) For the four models of (a) the energy density in the equatorial plane vs. the radial coordinate r, as in Fig. 17b.

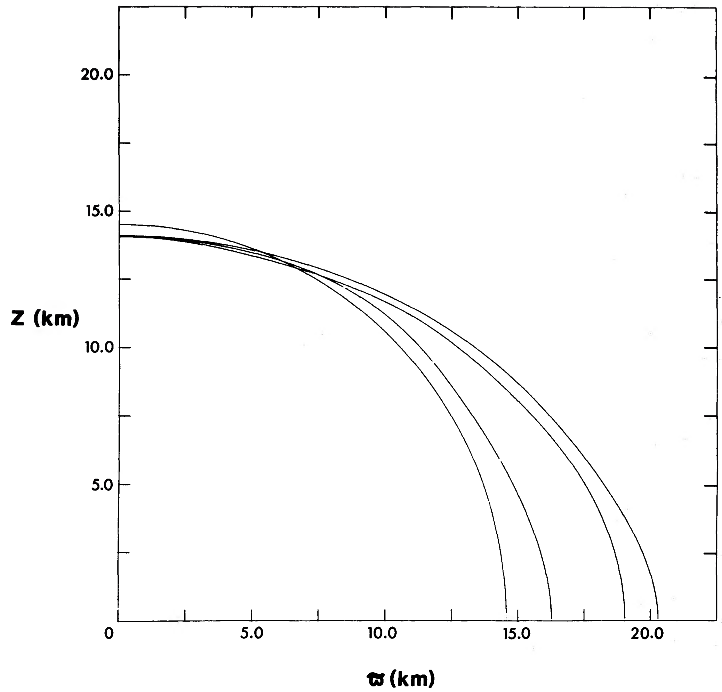

FIG. 20a

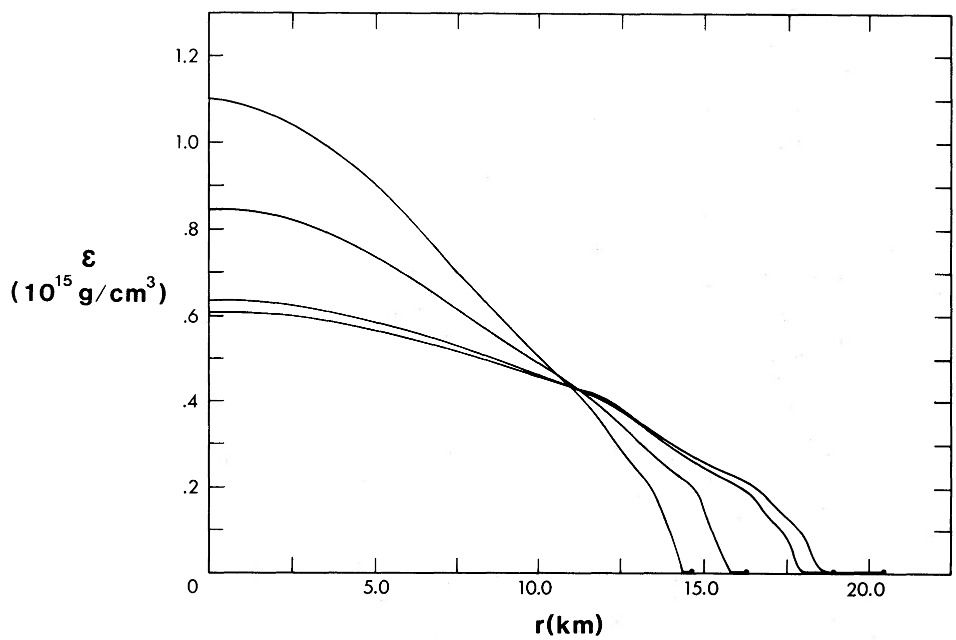

FIG. 20b

FIG. 20.—(a) The surfaces of four additional models based on EOS L(MF) depicted by embedding diagrams as in Fig. 16. For these models $\beta = 0.467 (M_0 \approx 2.7\ M_\odot)$; and $\Omega = 0$, $0.45 \times 10^4\ \mathrm{s}^{-1}$, $0.585 \times 10^4\ \mathrm{s}^{-1}$, and $0.60 \times 10^4\ \mathrm{s}^{-1} \approx \Omega_K$. ($b$) For the four models of (a) the energy density in the equatorial plane vs. the radial coordinate r, as in Fig. 17b.

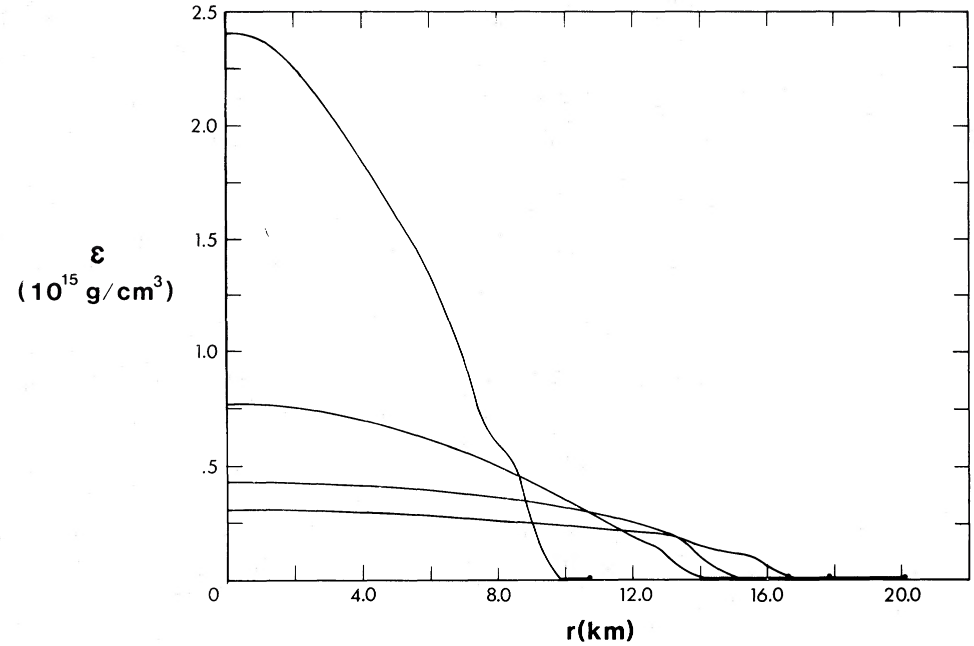

FIG. 21.—Energy density in the equatorial plane vs. the radial coordinate r for four models rotating with maximum angular velocity, $\Omega \approx \Omega_K$, and having rest mass $M_0 \approx 1.4\ M_\odot$. In order of increasing radius (or decreasing central density), the curves correspond to the following models, labeled by EOS, injection energy β, and angular velocity Ω: EOS G, $\beta = 0.54$, $\Omega = 1.005 \times 10^4\ s^{-1}$; EOS C(BJ I), $\beta = 0.676$, $\Omega = 0.574 \times 10^4\ s^{-1}$; EOS N*, $\beta = 0.715$, $\Omega = 0.482 \times 10^4\ s^{-1}$; EOS L(MF), $\beta = 0.756$, $\Omega = 0.383 \times 10^4\ s^{-1}$.

TABLE 8

MODELS AT TERMINATION POINTS FOR EQUATION OF STATE C(BJ I)

β	Ω	ϵ_c (10^{15} g cm^{-3})	$M/M_\odot$	$M_0/M_\odot$	R	ω_c/Ω	T/W	V_{eq}/c	I (10^{45} g cm^2)	cJ/GM^2	e	Z_p	Z_B	Z_F
0.811.........	0.413	0.506	0.783	0.814	18.3	0.249	0.071	0.25	0.87	0.62	0.77	0.11	0.41	−0.19
0.738.........	0.502	0.644	1.06	1.12	17.7	0.315	0.084	0.30	1.31	0.59	0.76	0.16	0.55	−0.21
0.676.........	0.573	0.773	1.29	1.39	16.9	0.402	0.093	0.32	1.69	0.57	0.74	0.22	0.67	−0.22
0.521.........	0.758	1.20	1.82	2.03	15.8	0.575	0.106	0.40	2.49	0.52	0.73	0.38	1.11	−0.27
0.446.........	0.869	1.58	2.03	2.29	15.1	0.650	0.110	0.44	2.68	0.50	0.72	0.50	1.41	−0.30
0.383.........	0.990	2.14	2.14	2.45	14.0	0.740	0.111	0.46	2.61	0.49	0.69	0.62	1.74	−0.31
0.372.........	1.017	2.30	2.15	2.46	13.6	0.755	0.110	0.46	2.56	0.49	0.69	0.64	1.80	−0.31
0.360.........	1.047	2.49	2.16	2.47	13.4	0.771	0.110	0.47	2.49	0.49	0.68	0.67	1.89	−0.33
0.352.........	1.071	2.64	2.16	2.47	13.2	0.783	0.110	0.48	2.44	0.49	0.68	0.68	1.94	−0.32
0.349.........	1.080	2.71	2.16	2.47	13.1	0.788	0.110	0.47	2.42	0.49	0.68	0.69	1.96	−0.31
0.330.........	1.144	2.14	2.14	2.44	12.1	0.819	0.107	0.46	2.22	0.48	0.66	0.75	2.10	−0.30

TABLE 9

MODELS AT TERMINATION POINTS FOR EQUATION OF STATE F

β	Ω	ϵ_c (10^{15} g cm^{-3})	$M/M_\odot$	$M_0/M_\odot$	R	ω_c/Ω	T/W	V_{eq}/c	I (10^{45} g cm^2)	cJ/GM^2	e	Z_p	Z_B	Z_F
0.798.........	0.483	0.66	0.74	0.77	16.0	0.27	0.072	0.26	0.66	0.61	0.75	0.12	0.43	−0.19
0.721.........	0.585	0.85	1.01	1.07	15.5	0.35	0.086	0.30	1.00	0.59	0.75	0.18	0.58	−0.21
0.640.........	0.689	1.12	1.27	1.37	14.8	0.44	0.096	0.34	1.34	0.56	0.75	0.25	0.76	−0.24
0.541.........	0.841	1.81	1.53	1.69	14.0	0.56	0.100	0.39	1.54	0.52	0.74	0.36	1.04	−0.27
0.476.........	0.992	2.71	1.62	1.80	12.8	0.66	0.097	0.42	1.41	0.49	0.71	0.45	1.27	−0.29
0.460.........	1.035	2.99	1.62	1.80	11.7	0.65	0.096	0.40	1.34	0.49	0.69	0.47	1.31	−0.26
0.445.........	1.077	3.14	1.63	1.82	12.0	0.70	0.096	0.43	1.30	0.48	0.70	0.50	1.40	−0.29
0.435.........	1.104	3.55	1.64	1.84	11.8	0.71	0.095	0.42	1.28	0.48	0.69	0.52	1.44	−0.29
0.405.........	1.215	3.81	1.66	1.86	11.2	0.75	0.094	0.42	1.20	0.47	0.69	0.57	1.60	−0.30
0.390.........	1.245	4.12	1.66	1.87	10.7	0.77	0.094	0.44	1.16	0.47	0.69	0.60	1.68	−0.29
0.370.........	1.317	4.63	1.66	1.86	10.5	0.80	0.093	0.46	1.09	0.47	0.68	0.64	1.80	−0.31
0.350.........	1.397	5.28	1.65	1.85	10.1	0.83	0.093	0.47	1.02	0.47	0.67	0.69	1.93	−0.32
0.340.........	1.441	5.70	1.64	1.84	9.8	0.84	0.093	0.47	0.98	0.48	0.67	0.71	2.00	−0.32

TABLE 10

Models at Termination Points for Equation of State G

β	Ω	ϵ_c (10^{15} g cm^{-3})	$M/M_\odot$	$M_0/M_\odot$	R	ω_c/Ω	T/W	V_{eq}/c	I (10^{45} g cm^2)	cJ/GM^2	e	Z_p	Z_B	Z_F
0.84.........	0.473	0.79	0.51	0.53	13.3	0.22	0.051	0.23	2.99	0.61	0.73	0.09	0.34	−0.16
0.79.........	0.570	1.08	0.66	0.69	12.6	0.28	0.064	0.27	4.26	0.62	0.74	0.12	0.44	−0.18
0.74.........	0.645	1.31	0.80	0.84	11.4	0.34	0.067	0.28	5.19	0.59	0.70	0.16	0.51	−0.17
0.64.........	0.810	1.75	1.04	1.13	10.8	0.46	0.076	0.29	6.96	0.59	0.69	0.25	0.71	−0.19
0.60.........	0.870	1.99	1.16	1.27	10.7	0.50	0.079	0.31	7.90	0.57	0.68	0.29	0.81	−0.19
0.57.........	0.930	2.17	1.22	1.34	10.5	0.53	0.084	0.33	8.30	0.59	0.68	0.32	0.90	−0.21
0.54.........	1.005	2.39	1.28	1.41	10.3	0.57	0.087	0.34	8.70	0.59	0.69	0.36	1.00	−0.22
0.49.........	1.095	2.85	1.37	1.53	10.2	0.63	0.092	0.37	9.16	0.60	0.68	0.43	1.18	−0.24
0.41.........	1.296	3.74	1.49	1.68	9.6	0.72	0.099	0.41	9.43	0.61	0.68	0.56	1.56	−0.28
0.37.........	1.416	4.55	1.53	1.71	9.1	0.77	0.101	0.43	9.08	0.61	0.67	0.64	1.79	−0.29
0.34.........	1.524	5.48	1.55	1.73	8.6	0.81	0.101	0.43	8.66	0.62	0.65	0.71	2.01	−0.29
0.32.........	1.611	6.37	1.53	1.71	8.3	0.83	0.099	0.50	7.80	0.62	0.65	0.77	2.16	−0.29

modes. Two estimates are made, using results of Lindblom (1985) and of Managan (1985), and the predicted growth times are similar.

Lindblom has computed the damping time τ and real frequency σ of normal modes with $l = m$ for spherical stars of rest mass $M_0 = 1.4\ M_\odot$, and based on the EOSs we consider here. For slow rotation, he observes that σ is related to the frequency σ_0 of the spherical star by

$$\sigma = \sigma_0 - \alpha m \Omega \ , \tag{24}$$

where α is a constant smaller than 1. For $\Omega \gtrsim \sigma_0/m$, the frequency is negative and the mode is unstable, with a growth time on the order of

$$\tau = \tau_0 \, | \sigma_0/\sigma |^{2m+1} \ .$$

Extrapolating equation (24) to a neighborhood of the instability point $\Omega = \Omega_m$, where σ vanishes, we have

$$\sigma \approx m\alpha(\Omega - \Omega_m) \ ,$$

and $\Omega \leq \Omega_K$ implies

$$\sigma \leq m(\Omega_K - \Omega_m) \ .$$

Then the growth time is given approximately by

$$\tau_m \gtrsim \tau_0 \left[\frac{\sigma_0}{m(\Omega_K - \Omega_m)} \right]^{2m+1} \ . \tag{25}$$

With $\Omega_4 \geq \Omega(t = 0.04)$ (from the Newtonian results quoted above), we have $\tau_4 \geq 10^7$ s; the more probable value, $\Omega_4 \approx \Omega(t = 0.06)$, implies $\tau_4 \gtrsim 10^9$ s. Similarly, $\Omega_3 \geq \Omega(t = 0.06)$ implies $\tau_3 \geq 10^6$ s, and the more probable value, $\Omega_3 \approx \Omega(t = 0.08)$, implies $\tau_3 \gtrsim 10^8$ s.

A second estimate is based on Managan's (1985) quasi-Newtonian analysis. In the absence of viscosity, he finds the frequency of oscillation σ_m and the growth time scale τ_m for the unstable m-mode are given by

$$\sigma_m = \sigma_m^* \tilde{M}^{-1} \tilde{\Phi}_p^{3/2}\ \mathrm{s}^{-1} \tag{26}$$

and

$$\tau_m = \left(\frac{\sigma_m^*}{1500} \right)^{-(2m+1)} \tau^* \tilde{M} \tilde{\Phi}_p^{-(m+2)}\ \mathrm{s} \ . \tag{27}$$

Here $\tilde{M}$ is the mass in units of $1.4\ M_\odot$ and $\tilde{\Phi}_p$ is the polar gravitational potential in units of $0.15c^2$. The quantity σ_m^* is related to the amount Δt by which the actual value of t exceeds the critical value for no viscosity. For $0.5 \lesssim n \neq 1$, the data in Managan's Table 2 imply that

$$\sigma_m^* \approx \begin{bmatrix} 9.5 \times 10^4 \\ 1.5 \times 10^5 \end{bmatrix} \Delta t \tag{28}$$

and

$$\tau_m^* \approx \begin{bmatrix} (4 + 6n^2) \times 10^6 \\ [1 + (3/2)n^2] \times 10^{11} \end{bmatrix} . \tag{29}$$

TABLE 11

Models at Termination Points for Equation of State L(MF)

β	Ω	ϵ_c (10^{15} g cm^{-3})	$M/M_\odot$	$M_0/M_\odot$	R	ω_c/Ω	T/W	V_{eq}/c	I (10^{45} g cm^2)	cJ/GM^2	e	Z_p	Z_B	Z_F
0.756.........	0.383	0.311	1.23	1.32	19.1	0.298	0.076	0.270	2.53	0.73	0.76	0.15	0.49	−0.18
0.74..........	0.398	0.324	1.32	1.41	19.9	0.315	0.081	0.293	2.83	0.73	0.76	0.16	0.53	−0.19
0.70..........	0.428	0.369	1.53	1.66	20.3	0.360	0.089	0.323	3.55	0.73	0.76	0.20	0.61	−0.21
0.66..........	0.458	0.414	1.73	1.89	20.0	0.405	0.094	0.343	4.14	0.72	0.74	0.23	0.70	−0.21
0.62..........	0.488	0.444	1.94	2.13	20.0	0.449	0.100	0.325	4.78	0.71	0.74	0.27	0.79	−0.22
0.58..........	0.518	0.472	2.15	2.39	20.0	0.522	0.106	0.382	5.54	0.71	0.74	0.31	0.91	−0.23
0.54..........	0.548	0.504	2.37	2.66	20.1	0.533	0.111	0.415	6.39	0.71	0.74	0.36	1.04	−0.25
0.50..........	0.578	0.533	2.58	2.93	20.0	0.575	0.113	0.433	7.06	0.70	0.73	0.41	1.18	−0.25
0.46..........	0.608	0.610	2.78	3.21	19.6	0.629	0.115	0.471	7.86	0.70	0.72	0.47	1.34	−0.26
0.42..........	0.645	0.707	2.98	3.47	18.8	0.668	0.118	0.480	8.43	0.70	0.71	0.54	1.54	−0.27
0.38..........	0.694	0.879	3.10	3.63	18.0	0.718	0.119	0.496	8.33	0.68	0.69	0.62	1.76	−0.28
0.36..........	0.725	0.983	3.14	3.68	17.6	0.743	0.119	0.509	8.10	0.68	0.69	0.67	1.90	−0.28
0.34..........	0.764	1.11	3.18	3.72	17.3	0.767	0.122	0.526	7.87	0.68	0.69	0.71	2.07	−0.30
0.33..........	0.786	1.27	3.16	3.70	16.7	0.785	0.116	0.500	7.30	0.65	0.68	0.74	2.17	−0.28
0.32..........	0.807	1.33	3.14	3.70	16.3	0.793	0.114	0.490	7.03	0.65	0.68	0.77	2.31	−0.27

In these and in the following equations the upper entry refers to $m = 3$ and the lower to $m = 4$. We now have

$$\sigma_m \approx \begin{bmatrix} 2 \times 10^3 \\ 3 \times 10^3 \end{bmatrix} \left(\frac{\Delta t}{0.02}\right) \tilde{M}^{-1} \tilde{\Phi}_p^{3/2} \text{ s}^{-1} \tag{30}$$

and

$$\tau_m \approx \begin{bmatrix} 2 \times 10^6 \\ 4 \times 10^8 \end{bmatrix} \left(\frac{\Delta t}{0.02}\right)^{-(2m+1)} \tilde{M} \Phi_p^{-(m+2)} . \tag{31}$$

Using $t_3 \approx 0.08$ and $t_4 \approx 0.06$ again yields growth times ranging from months to years.

In the presence of viscosity, these modes will be unstable only when τ_m above is less than the viscous damping time (cf. Comins 1979),

$$\tau_{v,m} \approx 10^9 R_{15}^2 \nu_{100}^{-1} \text{ s} . \tag{32}$$

Here R_{15} is the equatorial radius in units of 15 km, and ν_{100} is the viscosity in units of 100 $\text{cm}^2 \text{ s}^{-1}$. This value of viscosity conforms to the calculations of Flowers and Itoh (1976, 1979) when $T = 10^9$ K. For smaller T, the viscosity is larger, with expected dependence $\nu \propto T^{-2}$ in a superfluid interior. There is, however, substantial uncertainty in estimating viscosity and consequently in deciding when the gravitational radiation instability will be important. In particular, a large effective bulk viscosity might arise from hyperon production in the core (Langer and Cameron 1969).

Newly formed neutron stars maintain temperatures $T \gtrsim 10^9$ K for years, cooling to 10^8 K after $\sim 10^3$ yr. If rapidly rotating pulsars with weak magnetic fields can arise from collapse of white dwarfs, their rotation is therefore likely to be limited by the gravitational wave instability. For old accreting neutron stars, however, an expected temperature of 10^7 K appears to imply a viscous damping time in the range $10^5 \leq \tau \leq 10^9$ s (Wagoner 1984). When $\Omega \approx \Omega_K$, both the $m = 3$ and $m = 4$ modes may be unstable, but because of the uncertainty in ν, the question remains open.[2]

If the spread in the masses of actual neutron stars is not too large, one would expect the rotation frequencies of fast pulsars to stack up at the limiting value of Ω (cf. Friedman 1983). If $M_0 \approx 1.4\ M_\odot$, then, as discussed in § III, the limiting frequency ranges from $\sim 0.8 \times 10^4 \text{ s}^{-1}$ for EOS G to $\sim 0.55 \times 10^4 \text{ s}^{-1}$ for C(BJ I) to $0.4 \times 10^4 \text{ s}^{-1}$ for L(MF). The values increase with $M_\odot$ and with $T/|W|$.

b) *Axisymmetric Instability*

A second instability involves overall axisymmetric collapse. As noted earlier, for a given equation of state and for uniform rotation, this instability sets in (on a viscous time scale in general) along a sequence of fixed-angular-momentum configurations at the point where the mass peaks. In a plot of mass M versus radius R (cf. Figs. 5–8), the locus of such points is a line running from the peak of the $M(R)$ curve at zero angular momentum to the maximum-mass model for uniform rotation. If a configuration with baryon mass M_0 greater than the maximum value for nonrotating configurations spins down, for example by emission of magnetic dipole radiation, it will collapse when it reaches the line of instability in the $M(R)$ plot. We have not performed the calculations needed for determining precisely where the instability lies; but it is fairly evident from Figures 5–8 that a typical configuration near the onset of this instability has values of M and R ranging from $\sim 1.5\ M_\odot$ and 9 km for EOS G to $\sim 2\ M_\odot$ and 12 km for C to $\sim 3\ M_\odot$ and 16 km for L.

TABLE 12

STABILITY TERMINATION LIMITS FOR THE FAST PULSAR[a]

Equation of State	ϵ_c (10^{15} g cm^{-3})	$M/M_\odot$	R	I	Z_p
G.........	0.8	0.5	20	0.25	0.05
C.........	0.4	0.8	20	0.9	0.1
L.........	0.3	1.3	21	2.7	0.15

[a] All values are lower limits except that for R, which is an upper limit.

c) *Implications for the Fast Pulsar*

For a given equation of state and for uniform rotation, the observed stable angular velocity $\Omega_{\text{fp}} = 0.403 \times 10^4 \text{ s}^{-1}$ of the fast pulsar places limits on the values of various physical parameters describing its structure. (This has been noted already by Ray and Datta 1984.) Certainly $\Omega_{\text{fp}} < \Omega_K$, the value at sequence termination. We might also demand that the fast-pulsar value of $t \lesssim 0.8$, corresponding to the statement that the nonaxisymmetric modes are stable. In either case our results imply the same rough limits on structure parameters for the fast pulsar. These limits are obtained by extrapolation of the data in Tables 3–6 and are exhibited in Table 12, where all values are lower limits except that for R, which is an upper limit.

On the other hand, suppose we demand that the fast pulsar have baryon mass $M_0 \gtrsim 1.4\ M_\odot$. Then our results imply the approximate limits exhibited in Table 13. The values for ϵ_c, M, I, and Z_p are lower limits, while those for T/W and R are upper limits. Table 13 underscores the fact that the fast pulsar might be hovering at the nonaxisymmetric stability limit if its baryon mass $M_0 \approx 1.4\ M_\odot$ and if the correct EOS resembles L. Note from Figure 1 that for uniform rotation and for $M_0 \approx 1.4\ M_\odot$ the fast pulsar rules out all EOSs (e.g., M) that are significantly stiffer than L.

Of course, any of the proposed EOSs can be accommodated by increasing the fast pulsar's mass. For $\Omega = \Omega_{\text{fp}}$, there is a maximum possible mass for each EOS independent of stability considerations. Rough upper limits on the mass of the fast pulsar range from $\sim 1.5\ M_\odot$ for EOS G to $\sim 2\ M_\odot$ for C to $\sim 3\ M_\odot$ for L.

TABLE 13

MASS CONSTRAINT LIMITS FOR THE FAST PULSAR[a]

Equation of State	ϵ_c (10^{15} g cm^{-3})	$M/M_\odot$	R	T/W	I	Z_p
G.........	3	1.25	9	0.01	0.6	0.35
C.........	0.9	1.3	13	0.03	1.4	0.20
L.........	0.3	1.3	20	0.08	2.5	0.15

[a] The values for ϵ_c, M, I, and Z_p are lower limits. Those for T/W and R are upper limits.

[2] It has also been suggested (Blandford, Applegate, and Hernquist 1983) that magnetic fields on the order of 10^{12} G might arise spontaneously over a period of 10^5 yr as a young neutron star cools. If this were generally the case, the spin of neutron stars with white dwarf progenitors would be limited by the magnetic field, not by gravitational instability or the Keplerian velocity.

d) *Neutron Stars Spun Up via Accretion*

If its magnetic field is weak, a neutron star in a binary system might be spun up to a state of rapid rotation via accreting matter supplied by its companion star (Ghosh, Lamb, and Pethick 1977; Alpar *et al.* 1982; Backus, Taylor, and Damashek 1982). Wagoner (1984) has discussed the possible influence of the gravitational radiation driven instability on the evolution of such a neutron star. Here we shall briefly comment on the implications of our results for this phenomenon. If a neutron star is born with rest mass $M_0 \approx 1.4\ M_\odot$, then for the stiffer EOSs (C, O, N, L, and M) $R > 6GM/c^2 \approx 12$ km. In these cases we expect circular orbits in the accretion disk to be stable down to the stellar surface, because in the exterior Schwarzschild geometry, stable circular orbits extend down to $r = 6GM/c^2$. For models based on the remaining EOSs, circular orbits near the surface are unstable, and accreting matter will fall on the star with angular velocity smaller than that of a Keplerian orbit at the equator. Thus one might wonder whether accretion could succeed in spinning a neutron star up to its limiting frequency, if the EOS is soft.

We have examined the stability of circular orbits for the models based on EOSs G, FP, C, N, and L listed in this paper. For a stationary axisymmetric geometry in which the frequency of circular orbits is nonzero, a circular orbit is stable if and only if the angular momentum of an orbiting particle increases with increasing orbital radius (Bardeen 1971). We find that even for the softest EOS (G), as these models are spun up, the circular orbits stabilize: When $M \leq 1.4\ M_\odot$, stable circular orbits extend down to the stellar surface when $\Omega = \Omega_K$ for every EOS. For more massive models, however, stars with maximum frequency Ω_K *can* have unstable circular orbits. A rule consistent with all the models we tested is that at $\Omega = \Omega_K$ all circular orbits are stable when $\beta > 0.46$, while for $\beta < 0.40$ circular orbits near the surface are unstable. At $\Omega = \Omega_K$, only models based on the softest equations of state have unstable circular orbits when $M < 2M_\odot$. It is therefore unlikely that unstable circular orbits will play a role in the final state of an accreting neutron star, unless its initial mass substantially exceeds $1.4\ M_\odot$.

The neutron star may be spun up via accretion to the critical value t_3 or t_4 at onset of secular gravitational radiation instability in the presence of viscosity. If t momentarily exceeds the critical value, emission of gravitational radiation via the unstable mode will reduce t to the critical value on a growth time scale on the order of that given by equation (31). At this point the angular velocity of rotation Ω could lie anywhere between $\sim 0.4 \times 10^4$ and $1.5 \times 10^4\ \mathrm{s}^{-1}$, depending on the equation of state and the mass of the accreting neutron star. According to equation (30), the frequency σ_m of the nonaxisymmetric mode and of the associated gravitational waves could range up to $\sim 3 \times 10^3\ \mathrm{s}^{-1}$. This value is somewhat larger than that quoted by Wagoner (1984), who has estimated the strength of the waves.

Roughly the same values of Ω and σ_m are appropriate if the nonaxisymmetric secular instability is completely wiped out by viscosity damping and if the limit on rotation is now imposed by sequence termination at $\Omega = \Omega_K$. In this case the neutron star might deposit matter in a surrounding ring. Perhaps the ring is subject to nonaxisymmetric instabilities that enable the system to radiate away angular momentum efficiently.

Another interesting possibility is that accretion eventually increases the mass past the limit for stability against collapse. At this point the neutron star would collapse to a black hole. Typical values of cJ/GM^2, while less than unity, the maximum possible value for a Kerr black hole, are nonnegligible. Preliminary results of collapse calculations show the collapse might leave behind a significant ringlike distribution of matter (Stack 1984).

e) *Oblateness Effects in Pulsar Spindown*

Cowsik, Ghosh, and Melvin (1983) have studied how changes in oblateness affect the rate of spindown of a pulsar as it emits magnetic dipole radiation. Modeling neutron stars as Newtonian, Maclaurin spheroids, Cowsik *et al.* found that $\dot{P}$, the rate of change of pulsar period, does not increase monotonically with decreasing period P when changes in oblateness are allowed for. Rather, $\dot{P}$ reaches a maximum at a certain value of P of the order of a millisecond and then decreases by an order of magnitude as P is decreased further. In the same approximation, Cowsik *et al.* found essentially that, in our notation, the ratio $(\dot{M}/I\Omega\dot{\Omega})$ increases precipitously above unity at very small periods.

One can learn from extrapolation of the results in Tables 2–5 whether these effects carry over to realistic neutron stars. It turns out that the effects survive to some degree only if the equation of state is relatively soft. More specifically, consider models with $M_0 \approx 1.4\ M_\odot$. Compare configurations having nearly the maximum value of t along a sequence with configurations having values of t smaller by $\sim 20\%$, and use subscripts 1 and 2 to denote quantities associated with the former and latter configurations respectively. Since the rate of energy loss due to magnetic dipole radiation is proportional to Ω^4, note that

$$\dot{P} = -\frac{2\pi}{\Omega^2}\,\dot{\Omega} \approx -\frac{2\pi}{\Omega^2}\frac{\Delta\Omega}{\Delta M}\,\dot{M} \propto \frac{\Delta\Omega}{\Delta M}\,\Omega^2\ ,$$

where $\Delta\Omega$ and ΔM are changes along a fixed-M_0 sequence. Hence we find that $(\dot{P}_1/\dot{P}_2)$ ranges from ~ 0.4 for EOS G to ~ 0.8 for FP to ~ 1.3 for N; and that $(\dot{M}/I\Omega\dot{\Omega})_1/(\dot{M}/I\Omega\dot{\Omega})_2$ ranges from ~ 2.7 for G to ~ 1.3 for FP or for N.

In summary, for the softest proposed equations of state it is true that $\dot{P}$ should be smaller (by $\sim 50\%$) for the smallest possible periods than for somewhat larger periods, and that $(\dot{M}/I\Omega\dot{\Omega})$ should be larger (by $\sim 200\%$). But the effect diminishes fairly rapidly with increasing stiffness and essentially disappears for the stiffer equations of state.

We would like to thank S. Chandrasekar, R. Coldwell, S. Detweiler, L. Lindblom, J. P. Ostriker, V. R. Pandharipande, R. Sorkin, and R. V. Wagoner for helpful discussions in the course of this work. This research was funded in part by NSF grants PHY-8303597 and PHY-8441263.

REFERENCES

Alpar, M. A., Cheng, A. F., Ruderman, M. A., and Shaham, J. 1982, *Nature*, **302**, 124.
Arnett, W. D., and Bowers, R. L. 1974, *Publications in Astronomy*, Vol. **9**, *Neutron Star Structure: A Survey* (Department of Astronomy, University of Texas at Austin).
———. 1977, *Ap. J. Suppl.*, **33**, 415 (A-B).
Arponen, J. 1972, *Nucl. Phys.*, **A191**, 257.
Arons, J. 1983, *Nature*, **302**, 301.
Backus, P., Taylor, J., and Damashek, M. 1982, *Ap. J. (Letters)*, **225**, L63.
Bardeen, J. M. 1971, *Ap. J.*, **167**, 425.
Bardeen, J. M., and Wagoner, R. V. 1971, *Ap. J.*, **167**, 359.
Baumgart, D., and Friedman, J. L. 1985, *Proc. Roy. Soc. London*, in press.

Baym, G., and Pethick, C. 1979, *Ann. Rev. Astr. Ap.*, **17**, 415.
Baym, G., Pethick, C., and Sutherland, P. 1972, *Ap. J.*, **170**, 299.
Bethe, H. A., and Johnson, M. 1974, *Nucl. Phys.*, **A230**, 1.
Bonazzola, S., and Schneider, J. 1974, *Ap. J.*, **191**, 273.
Bowers, R. L., Gleeson, A. M., and Pedigo, R. D. 1975, *Phys. Rev.*, **D12**, 3043.
Blandford, R., Applegate, J., and Hernquist, T. 1983, *M.N.R.A.S.*, **204**, 1025.
Butterworth, E. M. 1976, *Ap. J.*, **204**, 561.
Butterworth, E. M., and Ipser, J. R. 1976, *Ap. J.*, **204**, 200.
Canuto, V., and Chitre, S. M. 1974, *Phys. Rev.*, **D9**, 1587.
Chandrasekhar, S. 1964, *Ap. J.*, **139**, 664.
———. 1970, *Phys. Rev. Letters*, **24**, 611.
Chandrasekhar, S., and Miller, J. C. 1974, *M.N.R.A.S.*, **167**, 63.
Comins, N. 1979, *M.N.R.A.S.*, **189**, 233.
Cowsik, R., Ghosh, P., and Melvin, M. A. 1983, *Nature*, **303**, 409.
Datta, B. 1984, *Nature*, **308**, 338.
Datta, B., and Kapoor, R. C. 1985, *Nature*, **315**, 557.
Datta, B., Kapoor, R. C., and Ray, A. 1984, *Bull. Astr. Soc. India*, **12**, 343.
Datta, B., and Ray, A. 1983, *M.N.R.A.S.*, **204**, 75P.
Detweiler, S. L., and Lindblom, L. 1977, *Ap. J.*, **213**, 193.
Durisen, R. H. 1975, *Ap. J.*, **183**, 215.
Fabian, A., Pringle, J., Verbunt, T., and Awade, P. 1983, *Nature*, **301**, 222.
Flowers, E., and Itoh, N. 1976, *Ap. J.*, **206**, 218.
———. 1979, *Ap. J.*, **230**, 847.
Friedman, B., and Pandharipande, V. R. 1981, *Nucl. Phys.*, **A361**, 502.
Friedman, J. L. 1978, *Comm. Math. Phys.*, **62**, 247.
———. 1983, *Phys. Rev. Letters*, **51**, 11.
Friedman, J. L., Ipser, J. R., and Parker, L. 1984, *Nature*, **312**, 255.
Friedman, J. L., Ipser, J. R., and Sorkin, R. 1986, in preparation.
Friedman, J. L., and Schutz, B. F. 1978, *Ap. J.*, **222**, 281.
Ghosh, P., Lamb, F. K., and Pethick, C. J. 1979, *Ap. J.*, **217**, 578.
Harding, A. K. 1983, *Nature*, **303**, 683.
Hartle, J. B. 1967, *Ap. J.*, **150**, 1005.
Hartle, J. B., and Friedman, J. L. 1975, *Ap. J.*, **272**, 702.
Hartle, J. B., and Thorne, K. S. 1968, *Ap. J.*, **153**, 807.
Imamura, J., Durisen, R., and Friedman, J. L. 1985, *Ap. J.*, **294**, 474.
James, R. A. 1964, *Ap. J.*, **140**, 552.
Kapoor, R. C., and Datta, B. 1984, *M.N.R.A.S.*, **209**, 895.
Langer, W. D., and Cameron, A. G. W. 1969, *Ap. Space Sci.*, **5**, 213.
Lindblom, L. 1984, *Ap. J.*, **278**, 364.
———. 1985, preprint.
Lindblom, L., and Detweiler, S. L. 1977, *Ap. J.*, **211**, 565.
Lindblom, L., and Hiscock, W. A. 1983, *Ap. J.*, **267**, 384.
Managan, R. 1985, *Ap. J.*, **294**, 463.
Misner, C. W., and Zapolsky, H. S. 1964, *Phys. Rev. Letters*, **12**, 635.
Moszkowski, S. 1974, *Phys. Rev.*, **D9**, 1613.
Negele, J., and Vautherin, D. 1973, *Nucl. Phys.*, **A207**, 298.
Pandharipande, V. R. 1971*a*, *Nucl. Phys.*, **A174**, 641.
———. 1971*b*, *Nucl. Phys.*, **A178**, 123.
Pandharipande, V. R., and Smith, R. A. 1975, *Nucl. Phys.*, **A175**, 225.
Papaloizou, J., and Pringle, J. E. 1978, *M.N.R.A.S.*, **184**, 501.
Ray, A., and Chitre, S. M. 1983, *Nature*, **303**, 409.
Ray, A., and Datta, B. 1984, *Ap. J.*, **282**, 542.
Serot, B. D. 1979*a*, *Phys. Letters*, **86B**, 146.
———. 1979*b*, *Phys. Letters*, **87B**, 403.
Shapiro, S. L., and Lightman, A. P. 1976, *Ap. J.*, **207**, 263.
Shapiro, S. L., and Teukolsky, S. A. 1984, *Black Holes, White Dwarfs, and Neutron Stars* (New York: Wiley).
Shapiro, S. L., Teukolsky, S. A., and Wasserman, I. 1983, *Ap. J.*, **272**, 702.
Stack, R. 1984, private communication.
Stoeckly, R. 1965, *Ap. J.*, **142**, 208.
Tassoul, J. L. 1978, *Theory of Rotating Stars* (Princeton: Princeton University Press).
Thorne, K. S. 1967, in *High-Energy Astrophysics*, Vol. **3**, ed. C. DeWitt, E. Schatzman, and P. Veron (New York: Gordon and Breach), p. 259.
Wagoner, R. V. 1984, *Ap. J.*, **278**, 345.
Walecka, J. D. 1974, *Ann. Phys.*, **83**, 491.
Wilson, J. R. 1972, *Ap. J.*, **176**, 195.

JOHN L. FRIEDMAN and LEONARD PARKER: Department of Physics, University of Wisconsin, Milwaukee, WI 53201

JAMES R. IPSER: Department of Physics, University of Florida, Gainesville, FL 32611